

**Texas A&M University
Mechanical Engineering Department
Turbomachinery Laboratory
Tribology Group**

Measurement of a Rotor (Dynamic) Axial Response in a Test Rig with Water Lubricated Hydrostatic Thrust Bearings

TRC-B&C-03-17

Research Progress Report to TAMU Turbomachinery Research Consortium

By

Luis San Andrés
Mast-Childs Chair Professor
Principal Investigator

Scott Wilkinson
Research Assistant

Syed Mohammad Hameed ul Haq
Research Assistant

March 2017

A Test Rig for Evaluation of Thrust Bearings and Face Seals

TRC Project, Maestro # 400124 00056

[Second Draft]

[Updated]

Executive Summary

A water lubricated thrust bearing test rig currently hosts two fixed geometry, tapered-land hydrodynamic thrust bearings. The test and slave thrust bearings impose equal and opposite forces to position the rotor axially. The 316 stainless steel rotor is a 197 mm long shaft with two thrust collars. The rotor is supported radially by two flexure-pivot, tilting pad journal bearings. A coupling connects the rotor to a 30 HP electric motor. A loading mechanism applies static and dynamic loading to the test thrust bearing through a non-rotating shaft. Aerostatic radial bearings enable this load shaft to move freely in the axial direction. As the test thrust bearing displaces to impose a load on the rotor, the slave TB reacts to this axial load.

This report discusses hydrostatic thrust bearing dynamic performance at moderate rotational speed (up to 6krpm). Water feeds the journal bearings at 50 psig and the thrust bearings at various supply pressure, max. 70 psig. At each water supply pressure into the thrust bearings, the load shaft and test TB applies a load onto the rotor thrust collar, the axial clearance decreasing as the axial load increases. The reduced clearance causes an increased flow resistance across the film lands of the thrust bearing, ultimately amounting to a reduced flow rate at a large axial load. As the flow rate decreases, the pressure drop across the orifice also decreases, which results in higher recess pressures. Therefore, as the axial load increases (axial clearance decreases) with a constant water lubricant supply pressure, the stiffness and damping increase. Also, with an increase in water supply pressure, thrust bearing stiffness and damping also increase. Added mass represents the fluid resistance incurred by the thrust bearing as it moves axially and is largely unaffected by rotor speed, bearing supply pressure or applied static load. With change in rotor speed, the hydrostatic bearing exhibits no appreciable change in axial forced performance. This is due to the lack of hydrodynamic features on the thrust bearing surface such as tapered sections or tilting pads.

As part of the 2016 TRC proposal, a hydrodynamic thrust bearing has been designed and manufactured. Two eight-pad hydrodynamic thrust bearing are designed with a land to taper area ratio of 1:1. The inner and outer diameter of the bearings is 40.6 mm and 76.2 mm, respectively. A straight taper with a height of 0.05 mm over a 10 mm region is used to produce a height difference between the start and end of the pad, a slider bearing configuration is achieved [1].

Nomenclature

α – Film Thickness Ratio

h_1 – Sum of axial clearance and minimum film thickness

h_2 – Minimum film thickness

z_{TTB} - Displacement of Test thrust bearing

z_R - Displacement of Rotor

K_{Cable} – Stiffness of the Cable

C_{TTB} – Damping Coefficient of test thrust bearing

K_{TTB} – Stiffness Coefficient of test thrust bearing

M_{TTB} – Added Mass Coefficient of test thrust bearing

$F_{d(t)}$ – Impact force applied to thrust bearing

F_{TTB0} – Thrust bearing reaction force due to static load

F_{Cable} - Force applied by the cable

M - Mass of the load shaft, TB and load cell.

\ddot{z}_{TTB} - Acceleration of test thrust bearing

F_{TTB} - Reaction of test thrust bearing

T_0 - Tension on the Cable

θ - Angle between cable and load shaft axis

$\bar{z}_{(\omega)}$ - Relative displacement of bearing in frequency domain

$\bar{A}_{(\omega)}$ - Acceleration of test thrust bearing in frequency domain

$H_{(\omega)}$ - Dynamic (complex) stiffness

$Re(H_{(\omega)})$ - Real part of Impedance function

$Im(H_{(\omega)})$ - Imaginary part of impedance function

$\bar{F}_{d(\omega)}$ - Impact force applied in frequency domain

C_0 - Axial gap at the center of the TB

δx - tilt of the rotor thrust collar about the x-axis

δy - tilt of the rotor thrust collar about the y-axis

X_{Si} - X coordinate of the proximity probe

Y_{Si} - Y coordinate of the proximity probe

R_2 - Outer Radius of bearing (in.)

R_1 - Inner Radius of bearing (in.)

W - Applied load (lb.)

k_g - fraction of area between R_1 and R_2 not used for feed grooves = 0.85

P - Unit load (psi)

L - Radial Length of the pad

R - Mean radius of the pad

ω - Rotational speed of the bearing

U - Surface speed

C_{pads} - circumference of total no. of pads

B - Pad width

K_h - Dimensionless film thickness coefficient

K_f - Dimensionless friction coefficient

K_q - Dimensionless flowrate coefficient

K_s - Dimensionless leakage coefficient

μ - Viscosity

E_p - Power Loss

Q_1 - Inlet flow rate

Q_s - Leakage flowrate of the bearing

Contents

Executive Summary	I
Nomenclature	II
List of Tables	2
List of Figures.....	2
Introduction	6
A Review of Hydrodynamic Thrust Bearings.....	7
Types of Hydrodynamic Thrust Bearings.....	8
Literature Review on Fixed Geometry Thrust Bearings.....	9
Description of Thrust Bearing Test Rig [20].....	14
Alignment Procedure	18
Static and Dynamic Load Application.....	19
Water Loop Startup and Adjustment	21
Motor Startup and Operation	22
Static Load Measurements.....	22
Impact Load Measurements.....	23
Thrust Bearing Dynamic Performance for Tests with Moderate Rotor Speed	24
Variable Rotor Speed.....	25
Variable Thrust Bearing Supply Pressure.....	27
Conclusion.....	30
References	31
Appendix A: Predictive Codes for Bearing Performance	34
References.....	36
Appendix B: Identification of Thrust Bearing Force Coefficients [B1]	37
References.....	40
Appendix C: Thrust Collar Plane Equation Derivation [C1]	41
REFERENCES	43
Appendix D: Hydrodynamic Thrust Bearing Design.....	44
Hydrodynamic Thrust Bearing Material.....	44
Bearing Design Calculations.....	45
Lubricant Feed Holes.....	49
Lubricant Grooves	49
Bearing Geometry.....	50
Operating Conditions.....	51
SolidWorks Models	53
Manufacturing Drawings	53
REFERENCES	55
Appendix E: Thrust Bearing Dynamic Coefficient Plots.....	56
Variable Rotor Speed Tests.....	57

Variable Thrust Bearing Supply Pressure.....	63
--	----

List of Tables

Table 1: Dimensions and physical parameters of flexure pivot pad radial hydrostatic bearing. Material: 330 Bronze.....	15
Table 2: Hydrodynamic Thrust Bearing Dimensions	17
Table 3: XLHydroJet Inputs and Outputs	34
Table 4: XLHydroThrust Inputs and Outputs	35
Table 5: Design Parameters for thrust bearings	46
Table 6: Section from Table of Performance Coefficients for Tapered-Land Thrust Bearings [E12].....	47
Table 7: Lubricant groove dimensions.....	49
Table 8: Hydrodynamic Thrust Bearings Parameters	50

List of Figures

Figure 1: Plane Slider Bearing working under hydrodynamic principle [1].....	7
Figure 2: Fixed Geometry and Tilting Pad Thrust Bearings [23]	8
Figure 3: SolidWorks Model showing Thrust Bearing Test Rig Housing and Air Pedestal ..	14
Figure 4: Depiction of water lubricated flexure pivot pad hydrostatic journal bearing [20].	16
Figure 5: Taper Land thrust bearings	17
Figure 6: View of Thrust Bearing Test Rig Schematic	18
Figure 7: LabView Visual Interface program for alignment.....	18
Figure 8: Air Pedestal Alignment movement.....	19
Figure 9: Loading Assembly for static and dynamic loading	20
Figure 10: Static Load Mechanism	20
Figure 11: Schematic diagram of closed loop water supply system for thrust bearing test-rig [3]	21
Figure 12. Example of the curve fitting procedure used to determine the force coefficients of the water lubricated test thrust bearing from the derived impedance function. The top plot represents the real part of impedance with respect to frequency squared ((rad/s) ²) where the stiffness and added mass are identified as intersection with the y-axis and the slope of the linear curve fit, respectively. The bottom plot represents the imaginary part of the impedance function with respect to frequency (rad/s) where the slope of the linear curve fit with intercept through the origin representing the identified damping of the system.....	24
Figure 13. Predicted and measured thrust bearing stiffness (N/m) for the test thrust bearing operating with water supplied at 70 psi(g) and shaft rotational speed of 3 krpm, 4krpm, 5krpm and 6krpm. Journal bearings supplied with water at 50 psi(g) support the rotor. The frequency range used for identification is 0-250 Hz based on coherence. 100 impact tests, each consisting of 16,386 samples recorded with a sampling frequency of 31,250 Hz, are averaged.....	25
Figure 14. Predicted and measured thrust bearing damping (Ns/m) for the test thrust bearing operating with water supplied at 70 psi(g) and shaft rotational speed of 3 krpm, 4krpm, 5krpm and 6krpm. Journal bearings supplied with water at 50 psi(g) support the rotor. The frequency range used for identification is 0-250 Hz based on coherence. 100 impact tests, each consisting of 16,386 samples recorded with a sampling frequency of 31,250 Hz, are averaged.....	26
Figure 15. Predicted and measured thrust bearing added mass (kg) for the test thrust bearing	

operating with water supplied at 70 psi(g) and shaft rotational speed of 3 krpm, 4krpm, 5krpm and 6krpm. Journal bearings supplied with water at 50 psi(g) support the rotor. The frequency range used for identification is 0-250 Hz based on coherence. 100 impact tests, each consisting of 16,386 samples recorded with a sampling frequency of 31,250 Hz, are averaged.....27

Figure 16. Predicted and measured thrust bearing stiffness (N/m) for the test thrust bearing operating with water supplied at 40, 50 and 60 psi(g) and shaft rotational speed of 3 krpm. Journal bearings supplied with water at 50 psi(g) support the rotor. The frequency range used for identification is 0-250 Hz based on coherence. 100 impact tests, each consisting of 16,386 samples recorded with a sampling frequency of 31,250 Hz, are averaged.27

Figure 17. Predicted and measured thrust bearing damping (Ns/m) for the test thrust bearing operating with water supplied at 40, 50 and 60 psi(g) and shaft rotational speed of 3 krpm. Journal bearings supplied with water at 50 psi(g) support the rotor. The frequency range used for identification is 0-250 Hz based on coherence. 100 impact tests, each consisting of 16,386 samples recorded with a sampling frequency of 31,250 Hz, are averaged.28

Figure 18. Predicted and measured thrust bearing added mass (kg) for the test thrust bearing operating with water supplied at 40, 50 and 60 psi(g) and shaft rotational speed of 3 krpm. Journal bearings supplied with water at 50 psi(g) support the rotor. The frequency range used for identification is 0-250 Hz based on coherence. 100 impact tests, each consisting of 16,386 samples recorded with a sampling frequency of 31,250 Hz, are averaged.29

Figure 19: Schematic view of 1-DOF model of test TB for parameter identification.37

Figure 20: Reference diagram of a thrust bearing for geometric calculation for Location of Proximity Probes41

Figure 21: Fixed Geometry Tapered Land Thrust Bearing [E6].....45

Figure 22: Thrust Bearing and Runner (E12).....45

Figure 23: Preliminary Sketch for Hydrodynamic Thrust Bearing [E5] – All units in mm ...50

Figure 24: Minimum Film Thickness and Lubricant Flow Rate Plots vs Rotor Speed for Hydrodynamic Test Thrust Bearing52

Figure 25: Test Thrust Bearing SolidWorks Model.....53

Figure 26: Test Thrust Bearing Detail Drawings54

Figure 23: Measured (a) thrust bearing stiffness (N/m), added mass (kg) and (b) damping for the test thrust bearing operating with water supplied at 70 psi(g), static load of 40 lbf. and shaft rotational speed of 3 krpm. Journal bearings supplied with water at 50 psi(g) support the rotor. The frequency range used for identification is 0-250 Hz based on coherence. 100 impact tests, each consisting of 16,386 samples recorded with a sampling frequency of 31,250 Hz, are averaged **Error! Bookmark not defined.**

Figure 24: Measured (a) thrust bearing stiffness (N/m), added mass (kg) and (b) damping for the test thrust bearing operating with water supplied at 70 psi(g), static load of 50 lbf. and shaft rotational speed of 3 krpm. Journal bearings supplied with water at 50 psi(g) support the rotor. The frequency range used for identification is 0-250 Hz based on coherence. 100 impact tests, each consisting of 16,386 samples recorded with a sampling frequency of 31,250 Hz, are averaged **Error! Bookmark not defined.**

Figure 25: Measured (a) thrust bearing stiffness (N/m), added mass (kg) and (b) damping for the test thrust bearing operating with water supplied at 70 psi(g), static load of 60 lbf. and shaft rotational speed of 3 krpm. Journal bearings supplied with water at 50 psi(g) support the rotor. The frequency range used for identification is 0-250 Hz based on coherence. 100 impact tests, each consisting of 16,386 samples recorded with a sampling frequency of 31,250 Hz, are averaged **Error! Bookmark not defined.**

Figure 26: Measured (a) thrust bearing stiffness (N/m), added mass (kg) and (b) damping (for

the test thrust bearing operating with water supplied at 70 psi(g), static load of 40 lbf. and shaft rotational speed of 4 krpm. Journal bearings supplied with water at 50 psi(g) support the rotor. The frequency range used for identification is 0-250 Hz based on coherence. 100 impact tests, each consisting of 16,386 samples recorded with a sampling frequency of 31,250 Hz, are averaged **Error! Bookmark not defined.**

Figure 27: Measured (a) thrust bearing stiffness (N/m), added mass (kg) and (b) damping (for the test thrust bearing operating with water supplied at 70 psi(g), static load of 50 lbf. and shaft rotational speed of 4 krpm. Journal bearings supplied with water at 50 psi(g) support the rotor. The frequency range used for identification is 0-250 Hz based on coherence. 100 impact tests, each consisting of 16,386 samples recorded with a sampling frequency of 31,250 Hz, are averaged **Error! Bookmark not defined.**

Figure 28: Measured (a) thrust bearing stiffness (N/m), added mass (kg) and (b) damping (for the test thrust bearing operating with water supplied at 70 psi(g), static load of 60 lbf. and shaft rotational speed of 4 krpm. Journal bearings supplied with water at 50 psi(g) support the rotor. The frequency range used for identification is 0-250 Hz based on coherence. 100 impact tests, each consisting of 16,386 samples recorded with a sampling frequency of 31,250 Hz, are averaged **Error! Bookmark not defined.**

Figure 29: Measured (a) thrust bearing stiffness (N/m), added mass (kg) and (b) damping (for the test thrust bearing operating with water supplied at 70 psi(g), static load of 40 lbf. and shaft rotational speed of 5 krpm. Journal bearings supplied with water at 50 psi(g) support the rotor. The frequency range used for identification is 0-250 Hz based on coherence. 100 impact tests, each consisting of 16,386 samples recorded with a sampling frequency of 31,250 Hz, are averaged **Error! Bookmark not defined.**

Figure 30: Measured (a) thrust bearing stiffness (N/m), added mass (kg) and (b) damping (for the test thrust bearing operating with water supplied at 70 psi(g), static load of 50 lbf. and shaft rotational speed of 5 krpm. Journal bearings supplied with water at 50 psi(g) support the rotor. The frequency range used for identification is 0-250 Hz based on coherence. 100 impact tests, each consisting of 16,386 samples recorded with a sampling frequency of 31,250 Hz, are averaged **Error! Bookmark not defined.**

Figure 31: Measured (a) thrust bearing stiffness (N/m), added mass (kg) and (b) damping (for the test thrust bearing operating with water supplied at 70 psi(g), static load of 60 lbf. and shaft rotational speed of 5 krpm. Journal bearings supplied with water at 50 psi(g) support the rotor. The frequency range used for identification is 0-250 Hz based on coherence. 100 impact tests, each consisting of 16,386 samples recorded with a sampling frequency of 31,250 Hz, are averaged **Error! Bookmark not defined.**

Figure 32: Measured (a) thrust bearing stiffness (N/m), added mass (kg) and (b) damping (for the test thrust bearing operating with water supplied at 70 psi(g), static load of 40 lbf. and shaft rotational speed of 6 krpm. Journal bearings supplied with water at 50 psi(g) support the rotor. The frequency range used for identification is 0-250 Hz based on coherence. 100 impact tests, each consisting of 16,386 samples recorded with a sampling frequency of 31,250 Hz, are averaged **Error! Bookmark not defined.**

Figure 33: Measured (a) thrust bearing stiffness (N/m), added mass (kg) and (b) damping (for the test thrust bearing operating with water supplied at 70 psi(g), static load of 50 lbf. and shaft rotational speed of 6 krpm. Journal bearings supplied with water at 50 psi(g) support the rotor. The frequency range used for identification is 0-250 Hz based on coherence. 100 impact tests, each consisting of 16,386 samples recorded with a sampling frequency of 31,250 Hz, are averaged **Error! Bookmark not defined.**

Figure 34: Measured (a) thrust bearing stiffness (N/m), added mass (kg) and (b) damping (for

the test thrust bearing operating with water supplied at 70 psi(g), static load of 60 lbf. and shaft rotational speed of 6 krpm. Journal bearings supplied with water at 50 psi(g) support the rotor. The frequency range used for identification is 0-250 Hz based on coherence. 100 impact tests, each consisting of 16,386 samples recorded with a sampling frequency of 31,250 Hz, are averaged**Error! Bookmark not defined.**

Introduction

In rotating machinery, thrust bearings (TB) support axial loads and control shaft position.

In centrifugal compressors, for example, axial loads depend on shaft speed, gas composition and physical properties, and operating pressure. The prediction of (impeller shroud) axial loads is largely empirical, creating the need for reliable TBs [2].

For the purpose of enhancing thrust bearing technology, Texas A&M Turbomachinery Laboratory developed a prediction tool to predict the performance of thrust bearings. The USAF (2006-2009) supported the design and construction of a thrust bearing test rig which is used to validate the prediction tool [3]. Currently, the test rig will provide reliable experimental results for various types of thrust bearings. Measurements performed by Esser (2010) from the test hybrid thrust bearings exhibited remarkable correlation with results from a predictive tool [4]. In 2013, the thrust bearing test rig, modified to operate with air lubricated radial bearings, experienced large amplitude vibrations leading to severe damage with loss of parts [5]. The test rig, fully revamped and modified to operate with water as a lubricant, is now being used to measure the forced performance of water-lubricated thrust bearings operating at high supply pressure and high rotational speed [6].

This report presents performance of hydrostatic thrust bearing under impact loads at rotor speeds of up to 6000 RPM. Continuing with the previous work on hydrostatic thrust bearing (HTB) [3], the axial response derived from impact load conducted on an eight-pocket TB at a rotor speed of 3k and 6kprpm is hereby presented. In the future, other thrust bearing types and face seals will be assessed experimentally.

A Review of Hydrodynamic Thrust Bearings

Hydrodynamic thrust bearings are used in rotating machinery such as turbines, compressors, and pumps [7] where high stiffness and damping is required to balance axial excursions in horizontal shafts. They also have large scale applications where they are utilized in large hydrogenerators [8] to support vertical shafts. Classified as non-contact fluid film bearings, these bearings rely on fluid film pressure to provide support to large axial loads. Performance of these bearings largely depends on lubricant viscosity, surface speed, surface area, film thickness and geometry of the bearing [9].

Frene et al. [10] describe the working principles behind hydrodynamic thrust bearing operation. The authors consider a plane slider bearing configuration comprising of two non-parallel surfaces. Figure 1 shows the schematic of the configuration as horizontal surface moves with a certain velocity while the sloped surface remains stationary. The translational movement of the lower surface draws liquid into the wedge shaped clearance where a pressure field is developed when the lubrication is squeezed through a smaller gap, thus creating load capacity.

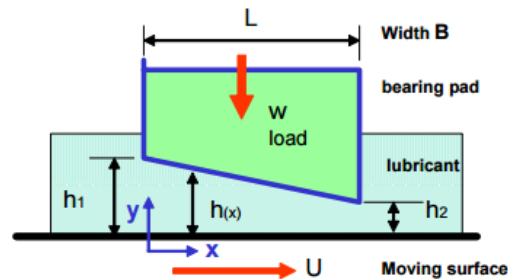


Figure 1: Plane Slider Bearing working under hydrodynamic principle [1]

Load capacity is significantly impacted by translational speeds of the horizontal surface, viscosity and the geometry of the bearing. At low speeds, with minimal hydrodynamic effect, load capacity is small and there is risk of bearing wear due to rubbing between the surfaces. At higher speeds, more liquid is drawn into the wedge, which increases the flow rate and subsequently the pressure across the wedge, and an increased ability to support the load of the moving surface [11]. Since pressure profile is also a function of geometry of bearing, it causes a change in load capacity. Pinkus and Sternlicht [12] define a film thickness ratio $\alpha = h_1/h_2$, where h_1 is the film thickness at the inlet of the wedge and h_2 is the minimum film thickness h_2 , as shown in fig. 1. At a film thickness ratio of 2.188, the load bearing capacity of a slider

bearing is maximum if all other factors remain constant. However, Frene et al. [10] state that as long as the departure from the plane of surface remains below half the minimum film thickness, variation in load capacity is negligible.

Types of Hydrodynamic Thrust Bearings

Hydrodynamic thrust bearings can be classified in two main types; fixed geometry and tilting pad bearing, as shown in Fig. 2. Fixed geometry bearings rely on the tapered section of the pad to produce load capacity while tilting pad bearings have moving pads that tilt to create a self-sustaining hydrodynamic film. Due to this ability to adapt to changing operating conditions with the tilting pads, performance of this types of bearing is dependent on a number of factors compared to fixed geometry bearings.

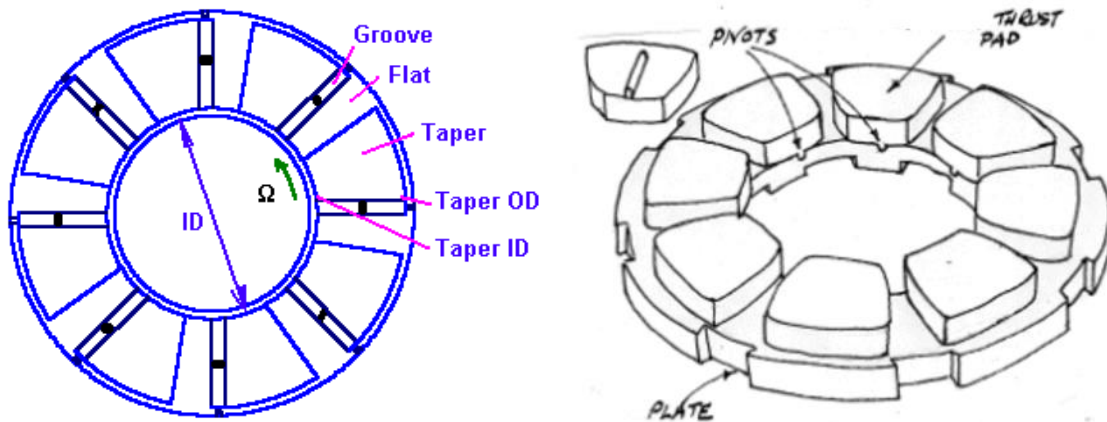


Figure 2: Fixed Geometry and Tilting Pad Thrust Bearings [23]

Fixed geometry thrust bearings are inexpensive to manufacture and best applied to constant load/speed applications and are optimized for a single application [13]. In comparison, tilting pad bearings are more versatile and provide load capacity at various speeds, adjusting the pads for each load/speed condition but are expensive to manufacture. Moreover, in practical applications, most equipment operates at fixed speed, making tapered-land bearing a viable option for a wide range of industrial applications. Applications with moderate specific pressures (up to 500 psi, 3.45 MPa) and relatively high speeds (1800 in/s, 45.72 m/s), tapered-land bearings perform ideally [14].

Literature Review on Fixed Geometry Thrust Bearings

Both types of bearings have an oil groove for lubricant inlet. Frene, J. (1978) [15] details a theoretical and experimental study conducted to show the effect of oil groove inclination on bearing performance characteristics. The study is performed for both the laminar and turbulent regimes where the turbulent conditions are modelled using Constantineusco's theory [24]. Changes in film thickness and flow regime on the bearing characteristics are also studied. A vertical test rig is used to measure bearing performance characteristics. Its speed ranges from 100 to 5000 RPM with a load applying capacity of up to 2000 N. The film thickness is measured using non-contacting displacement transducers. A six pad tapered land thrust bearing with a taper profile of 0.1 mm over a taper length of 25mm and oil grooves inclined at 30°, is tested to obtain experimental data for the study. The experimental results are compared with theoretical results to study the effects of inertial terms on bearing performance at a constant groove angle. The effect of the variation of groove angle on bearing performance is only studied theoretically. It is found that the groove angle has no significant effect on bearing performance from 0 to 50 degrees. After 50 degrees, a slight change is observed in flow rate and torque. The largest change occurs in load capacity with a change of about 20% over the next 15 degrees. Experimental and theoretical results are compared to see how the theoretical models hold up against experimental data. There is poor correlation between the theoretical and experimental results, possibly caused by poor misalignment of the thrust bearing. It is found from both experimental and theoretical data that torque values about the vertical axis are considerably affected as the flow regime changes.

Pinkus and Lund [16] study the effect of centrifugal forces on the hydrodynamics of high-speed thrust bearings. It is assumed that the flow regime is laminar and the fluid is incompressible with a variable viscosity field. For film thickness, two common geometries are considered including taper land thrust bearings and pivot shoe thrust bearing. The numerical analysis is based on a solution of a Navier Stokes equation. The Reynolds equations with centrifugal terms accounts for the inertia effects. Authors present a modified Reynolds number which signifies the presence of inertial effects in the Reynolds Equation. As this modified Reynolds number approaches zero, the inertial effects become negligible. The equations are solved by finite difference method.

The results obtained are normalized by the modified Reynolds number to represent the maximum impact of centrifugal effects on laminar operations of the bearings. The tapered land

thrust bearing will show a reduction in pressure and load capacity due to centrifugal effects. Also the variation in pad extent can cause a change in load capacity and flow. The centrifugal effects rise steeply with increase in pad extent. Therefore, scavenging of the lubricant from the bearing surface occurs at its inner radius, seriously affecting its load capacity. The variation in radial extent is performed at a certain pad extent value which shows that it is better to maintain a radial extent ratio greater than 0.55. The variation in angular slope does not have a significant impact on the load capacity, however, it has a significant impact on the flow rate. As the angular slope increases, a significant rise in flow rate is observed accounting for profound centrifugal effects on performance of bearing. It is found that with radial tapers, a very small area of the pad has negative centrifugal pressure results in a positive contribution to load capacity by the centrifugal forces. For positive contribution in load capacity, normalized taper should be greater than 0.65. Counter rotation is also an important consideration if centrifugal effects need to be minimized.

Hashimoto (1989) studies the fluid inertia effects caused by turbulent flow in sector pad thrust bearings [17]. For this purpose, momentum and continuity equations are used to model turbulent incompressible flow. A numerical calculation technique combining the control volume integration and the Newton-Raphson linearization method is applied to solve the equations. The results are categorized in four categories, solution with full inertia forces, solution with centrifugal forces only, solution without inertia forces, and solution by the conventional laminar theory. Load carrying capacity is compared for all four categories.

For a small film thickness ratio or a large pad extent angles, the negative effects of the centrifugal forces are superior to the positive effects of the convective inertia forces, thus the load carrying capacity decreases due to the combined inertia forces. On the other hand, for a large film thickness ratio or a small pad extent angle, the positive effects of the convective inertia forces are superior and the load carrying capacity increases due to the combined inertia forces. For a moderate film thickness ratio or a moderate pad extent angle, the positive effects of the convective inertia forces cancel the negative effects of the centrifugal forces, and the load carrying capacity is not influenced significantly by the combined inertia forces. For a certain Reynolds number and pad extent, the variation of load capacity shows that inclusion of inertia effects reduces the load capacity prediction. As the pad extent angle increase, the reduction in load capacity also increases.

Experimental results are obtained using a test rig with a rotating disk with four or six

sector shaped pads. The speed range of rotating disk is 20 to 330 RPS. The load is applied to the thrust collar by a lever. The film thickness is measured using contactless eddy current pressure transducers while temperature is measured at entrance and exit of bearing using thermocouples. Water is used as the lubricant. Experimental results show that load capacity reduction is visible in conditions when the bearing has a larger pad extent angle or a large pad width. At smaller pad extent angles, the reduction is almost negligible. This is because effects of the convective inertia forces cancel the negative effects of the centrifugal forces.

Dadouche, et. al. [7] present the effect of temperature variation across the bearing pads on the performance of the bearing incorporating effects of variations of oil viscosity in the oil film and thermal and elastic deformations of the bearing surfaces.

The theoretical analysis includes a solution of a thermohydrodynamic model of the bearing which is described by Reynolds equation, energy, and heat transfer equations. The experimental setup used for the analysis consisted of test thrust bearing: the sector-shaped pad ring and the collar attached to a rotating shaft. The test rig had a capability of going up to 2600 r/min and the maximum axial load of 8 kN. The lubricant used is ISO VG 32 and the bearing is flooded with lubricant. Lubricant film thickness is measured through three proximity probes located on the backing disc of the stator and K type thermocouples are placed behind the bearing surface to measure temperatures.

Experimental and theoretical results are compared showing relatively good correlations in all parameters studied. A temperature profile of a bearing pad is plotted showing variation in radial and circumferential direction. The highest pad temperature is observed at the outer radius of the pad and its trailing edge. This is an area with the minimum film thickness and maximum circumferential speed. It is observed that at constant shaft speed, a small variation in temperature is observed when load is increased. The results also indicate that the increase in pad temperature reaches 70% of the oil supply temperature at high load and high speed. While studying the change in pad temperature due to change in oil supply temperature, it is observed that the bearing supply temperature causes a change in bearing pad temperature from leading edge to trailing edge. Power Loss values are higher in experimental results because heat transferred through the metals is not accounted for. It is also reconfirmed that there is a significant contribution of oil leaking through the bleed grooves to the total bearing oil flow.

Henry et. al. [18] investigate a tapered land fixed geometry hydrodynamic thrust bearing. This type of bearing is not studied frequently enough compared to tilting pad thrust bearings

resulting in limited literature. The main focus of this paper is to enhance the understanding of hydrodynamic thrust bearing which can be later applied to help in reducing wear, friction, and damage to thrust bearings.

The test rig [18] can be described as having three essential components; the driving system, and a precision spindle, the loading system, a support to test the thrust bearing. Load is applied using a pneumatic jack monitored with a high-precision air regulator. This allows for a load variation between 50N and 8,000 N to be applied. The test rig is equipped with a tachometer for measuring the shaft speed, a force sensor for measuring the load, and a flowmeter and pressure probe to monitor the oil supply. A spherical hydrostatic thrust bearing is placed upstream of the test thrust bearing to keep this alignment regardless of the applied load. The pressure field is measured 90 deg. shifted from those pads and on two other opposite pads (also set at 180 deg. to each other), by using 12 pressure transducers per pad. The fixed geometry tapered land thrust bearing used for this study is composed of eight pads separated by eight grooves.

Results [18] indicated that an increase in the rotational speed and applied load leads to an increase in temperature at the interface. It is observed that an increase in the applied load leads to a higher pressure on the pad, while the rotational speed has only a weak influence on pressure. Also, the temperature gradient along the pad increases with load but even more with rotational speed. At low speed and low load, the pressure peak is located at the center of the pad. The pressure peak exhibits a slight tendency to move towards the trailing edge and inner radius of the pad when the applied load increases. This displacement can be attributed to both thermal and mechanical deformations of the thrust bearing components.

Song et. al. [19] studies cavitation effects in hydrodynamic tapered land thrust bearing and how it varies with different parameters of the bearing. For numerical analysis, centrifugal effects are very important because of the large radius variation across the oil film. A different form of the Reynolds equation including the centrifugal effects is used in our analysis. 3D Navier Stokes equation is also used along with a cavitation model because of limitations of Reynolds equation at locations such as the interface between the land area and the tapered area. Results obtained from these equations are compared with experimental data.

The test rig [19] is powered by a 37kW motor with rated speed of about 3000 rpm. A gear box with speed increasing ratio of 3.36 is added to study the bearing performance at higher rotational speeds up to 10,000 rpm. Lubricant used is ISO VG46 oil and a hydraulic piston is

used to load the bearing, and a spherical pivot is placed to ensure the alignment of the bearing with the collar. In order to visualize the bubbly flow, a technoscope is placed through the backing disk with an observation area in land.

The comparisons show a good qualitative agreement between results. Cavitation area always starts from the same location with various speeds, i.e., at the interface between adjacent pads, and then extends along the rotation direction. The parametric study showed that the load capacity decreases at higher speeds because of expansion of the cavitation area, which indicates the significant influence of cavitation on the bearing performance. And the negative effects of cavitation can be reduced at smaller film thickness and higher oil supply pressure.

Current literature does not present a reliable tool for predicting static and dynamic performance of fixed geometry thrust bearings. XLHydrothrust, developed at the Turbomachinery Lab at Texas A&M, is a complete tool for predicting performance of thrust bearings. It is currently being validated at the thrust bearing test rig.

Description of Thrust Bearing Test Rig [20]

The thrust bearing test rig has a face-to-face configuration with two hydrodynamic bearings facing each collar of the rotor. This configuration is similar to the back-to-back configuration used by Gardner [21] and Glavatskih [22] but with the thrust bearings facing the outer side of the rotor thrust disks. The bearings support a stainless steel rotor with two thrust collars on the drive end and free end. Hydrodynamic bearings provide an axial support to the rotor while the radial support is provided by two flexure pivot bearings. Figure 3 shows a model of the test rig with the face-to-face configuration and components including rotor and all four bearings.

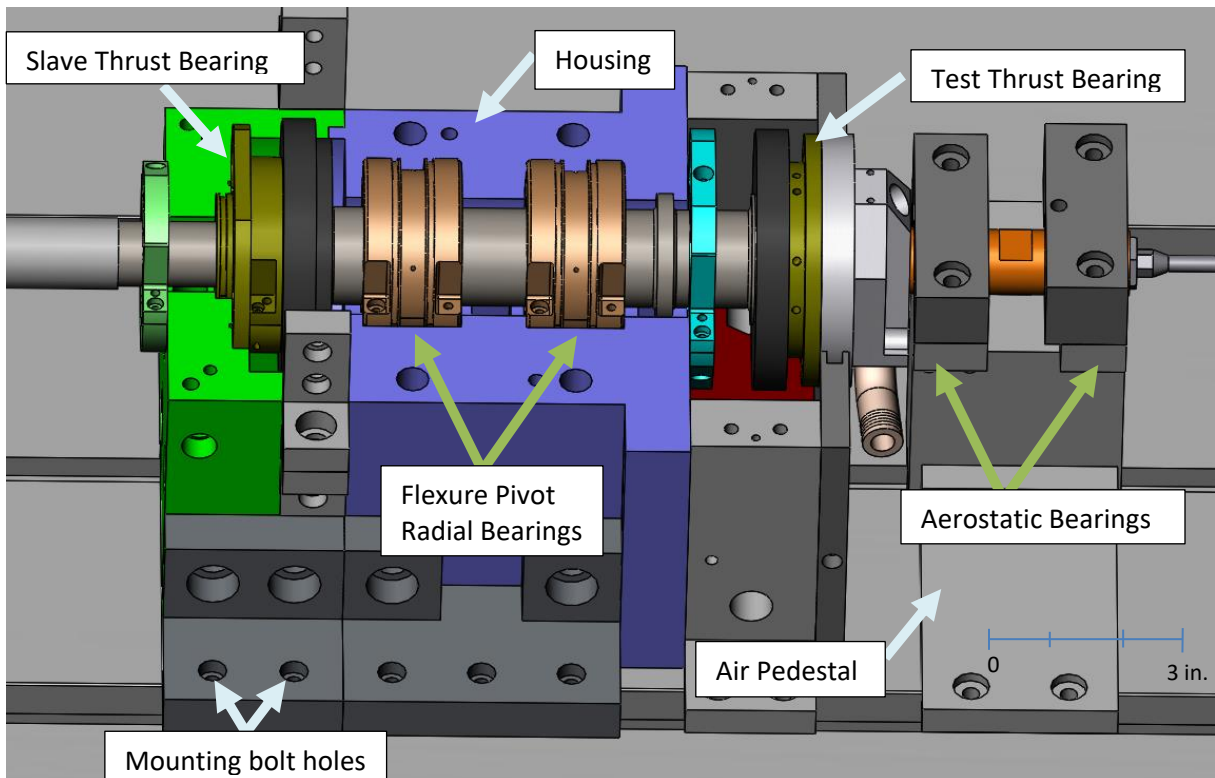


Figure 3: SolidWorks Model showing Thrust Bearing Test Rig Housing and Air Pedestal

A variable frequency drive is set up with the Thrust Bearing Test Rig. The electric drive motor is rated at 22 kW at a maximum operating speed of 30 krpm. The motor can deliver a constant torque, maximum 700 N-cm, over the entire speed range. A digital closed-loop speed control and a water chiller for cooling are included.

A flexure coupling with a quill shaft and hub clamp is installed between the motor and the rotor. The coupling has low axial stiffness (3.5N/mm) and allows for an axial travel of 0.61 to 1.21 mm. These characteristics permit isolating the motor from the axial loads imposed on

the thrust bearings.

The two axial support bearings are called slave thrust bearing (STB) and test thrust bearing (TTB), respectively. The slave thrust bearing is mounted onto the housing to provide a reaction to the load applied. The test TB is mounted on to an axial load shaft which is supported by aerostatic bearings supplied with filtered 10.34 bar (shop) air. These bearings produce high lateral stiffness and low friction, thus limiting radial motion and allowing for near friction free, precise load application. The load applied through the load shaft is transmitted to the rotor through the test TB. The axial displacement of the rotor is reacted by the slave TB through the second collar. This reaction stops the axial load from being transmitted to the motor which could be potentially dangerous.

Table 1: Dimensions and physical parameters of flexure pivot pad radial hydrostatic bearing. Material: 330 Bronze

Radial Face	Inner Diameter	1.5 inch (38.1 mm)
	Machined Radial Clearance	0.003 inch (0.076 mm)
Pads	Number of Pads	4
	Arc Length	72°
	Pivot Offset	60%
	Nominal Preload	20%
	Flexural Web Moment-angle Stiffness	200 N-m/rad
Pocket	Width	0.5 inch (12.7 mm)
One per pad	Arc Extent	24°
	Depth	20 mil (0.508 mm)
	Pocket/wetted area ratio	0.11
Orifice	Diameter,	0.067 inch (1.7 mm)
One per pocket	Radial Location	1.08 inch (27.4 mm)

Figure 4 shows radial bearing used in the test rig to support the rotor and Table 1 shows the physical parameters of the bearing. The radial bearing length and inner diameter equal 38.1 mm, with a machined radial clearance of 0.076 mm. It is made of Bronze 330 and flexure pivot – tilting pad type bearing (to avoid potential hydrodynamic instability induced by shaft rotation) with a load between pad configuration. Manufactured with a wired electrical discharge machining (EDM) process, it has four 72° arc pads with 60% pivot offset and 20% nominal preload. Each pad contains a pocket recess to supply pressurized fluid to fluid film generation. The pocket dimensions are 12.7 mm width, 24° arc extent, and 0.508 mm depth. The bearings are split in half for ease of installation. The ratio of pocket area to pad wetted area is 11% in accordance with accepted design practices for cryogenic liquid bearings [20].

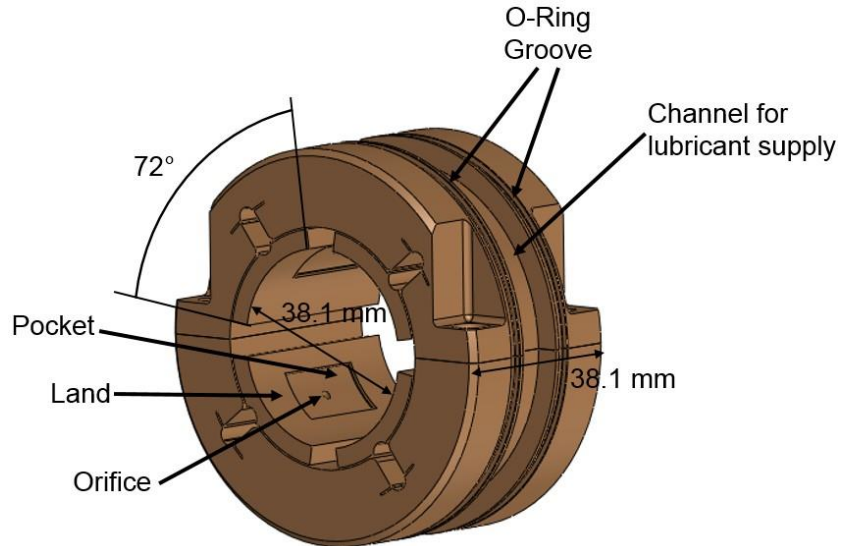


Figure 4: Depiction of water lubricated flexure pivot pad hydrostatic journal bearing [20].

Table 2: Hydrodynamic Thrust Bearing Dimensions

Thrust Face	Inner Diameter	40.6 mm
	Outer Diameter	76.2 mm
Pads	Number of Pads	8
	Pad width	17.8 mm
	Arc Length	19.9 mm
Taper	Taper height	0.05 mm
	Thrust to Resting Area Ratio	1:1
Oil Groove	Oil groove width [mm]	3 mm

Figure 5 shows the two hydrodynamic thrust bearings design for the test rig. These are fixed geometry tapered land thrust bearings. Appendix E details the design of these bearings.

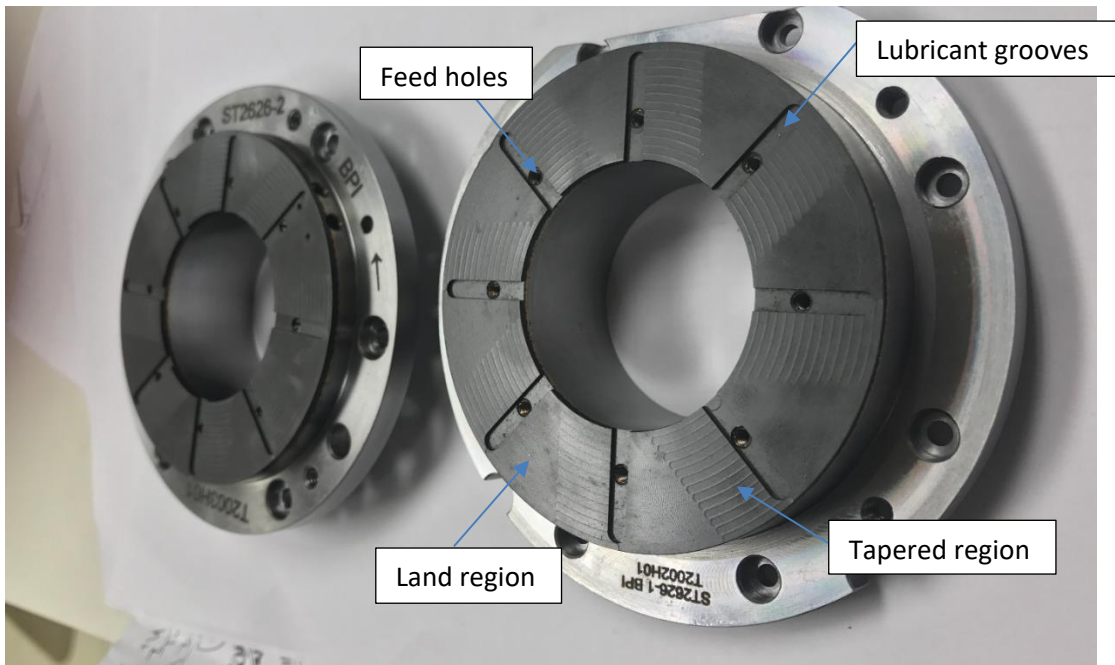


Figure 5: Taper Land thrust bearings

Figure 6 shows a schematic of the thrust bearing test rig showing the stiffness and damping models for the thrust and radial bearings. The spring represents the stiffness and dampers represent the damping generated by the bearing. Notice how the springs and dampers are reversed for the slave TB and test TB, depicting the face to face configuration of the test rig.

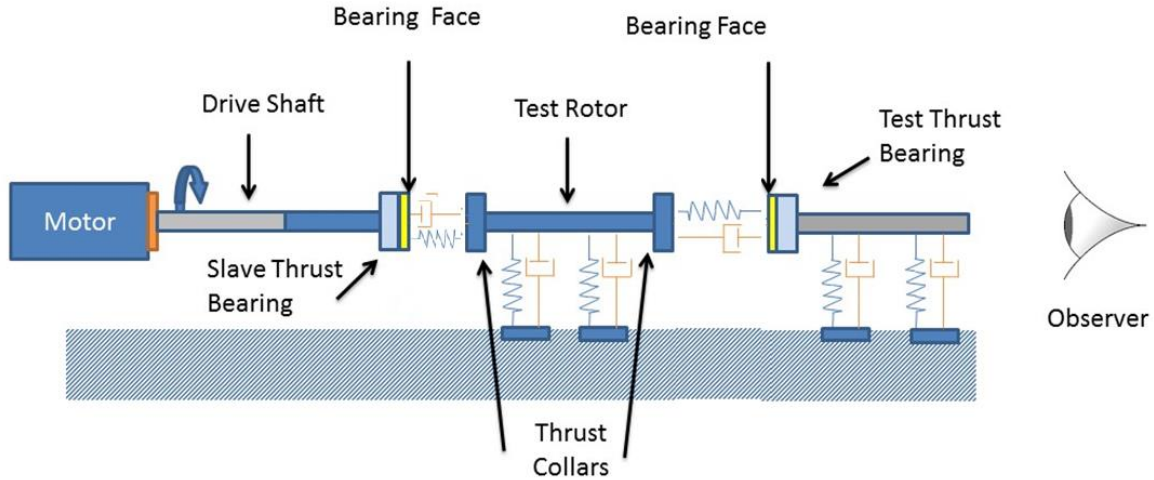


Figure 6: View of Thrust Bearing Test Rig Schematic

Testing Procedure for Thrust Bearing

Thrust bearing test rig is used to take measurements of thrust bearings under static and impact loads. Following sections describes a basic test procedure for both types of loads. The initial setup procedure for testing, are common for both types of loads.

Alignment Procedure

Current alignment procedure followed for the thrust bearing test rig is based on the three proximity probes set up for measuring axial clearance between thrust bearing and runner. A LabVIEW program uses the measurements from the probes as input. The program provides a dynamic output of horizontal and vertical movement needed to align the test thrust bearing with the runner. Figure 7 shows the alignment program.

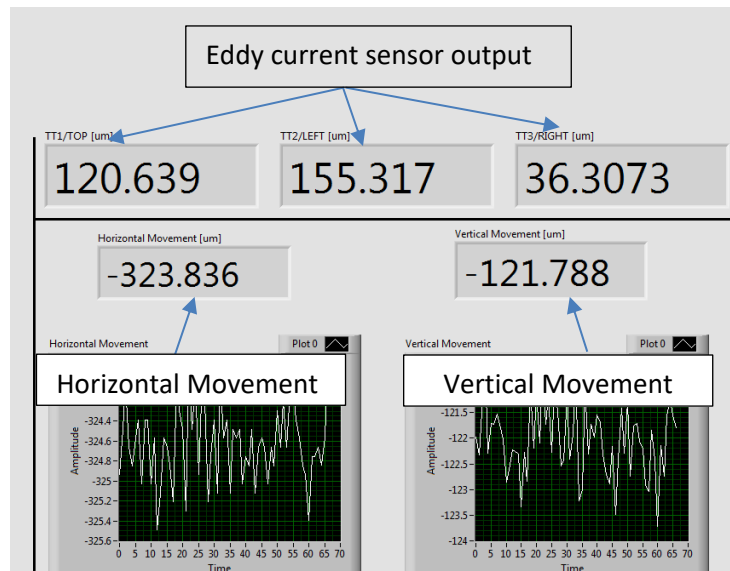


Figure 7: LabVIEW Visual Interface program for alignment

Based on the movement values from the program, the air pedestal is adjusted accordingly to complete the alignment. Figure 8 shows the adjustments motions to align the bearing with runner. Horizontal movement is catered by moving the pedestal horizontally, typically with impact. Tightening/loosening fixture bolts adjusts the vertical movement by lowering/raising the pedestal.

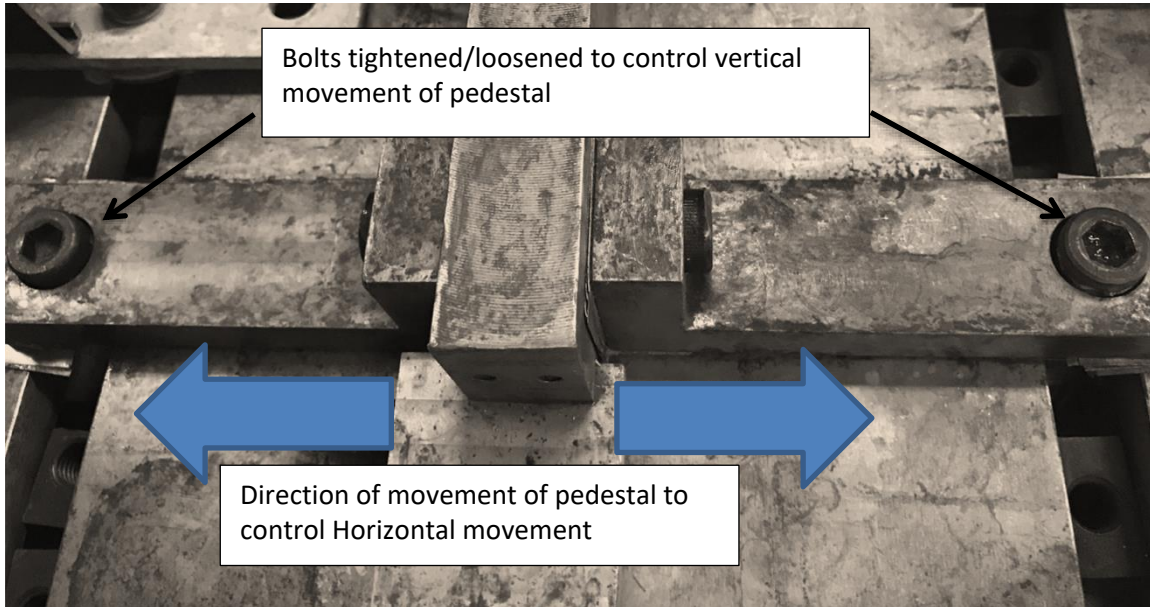


Figure 8: Air Pedestal Alignment movement

Static and Dynamic Load Application

Figure 10 shows the loading mechanism for the thrust bearing test rig. The static loading mechanism consists of the following

- Impact Gun
- Static Load Cell
- Cable
- Dynamic Load Cell
- Mounting Bracket
- Load Assembly

The dynamic load cell fastens directly to the load shaft and a shortened impact tip, (shown in fig. 9) was fabricated from steel. This arrangement will reduce weight, reduce the tilting effect from the loader and enable easier preloading of the dynamic load cell. The mass of the components pictured below amounts to 131.8g. The strain gauge load cell is mounted to a bracket which is bolted to the table. This arrangement

eliminates the effect of the sensor weight on the tension of the cable. Figure _ shows the impact tip which is connected to the load shaft.



Figure 9: Loading Assembly for static and dynamic loading

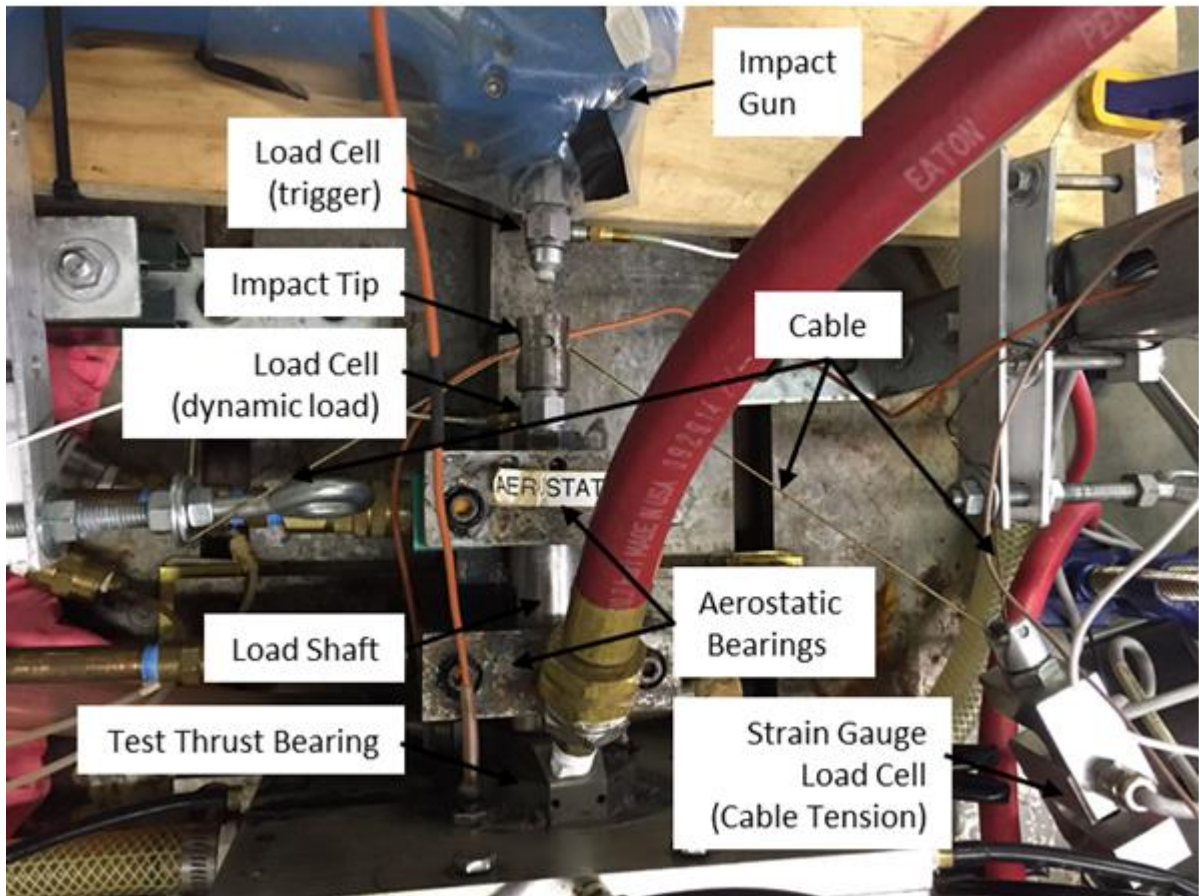


Figure 10: Static Load Mechanism

Water Loop Startup and Adjustment

Thrust bearing test rig currently uses water as a lubricant for its radial and thrust bearings. To provide a constant and adjustable water supply, a lubricant flow loop functions alongside the test rig.

Before entering the loop, water is passed through a Reverse Osmosis plant to remove contaminants that cause corrosion. Figure 11 shows the Main components of the water loop including main pump, a return pump, heat exchanger and a supply tank for storage.

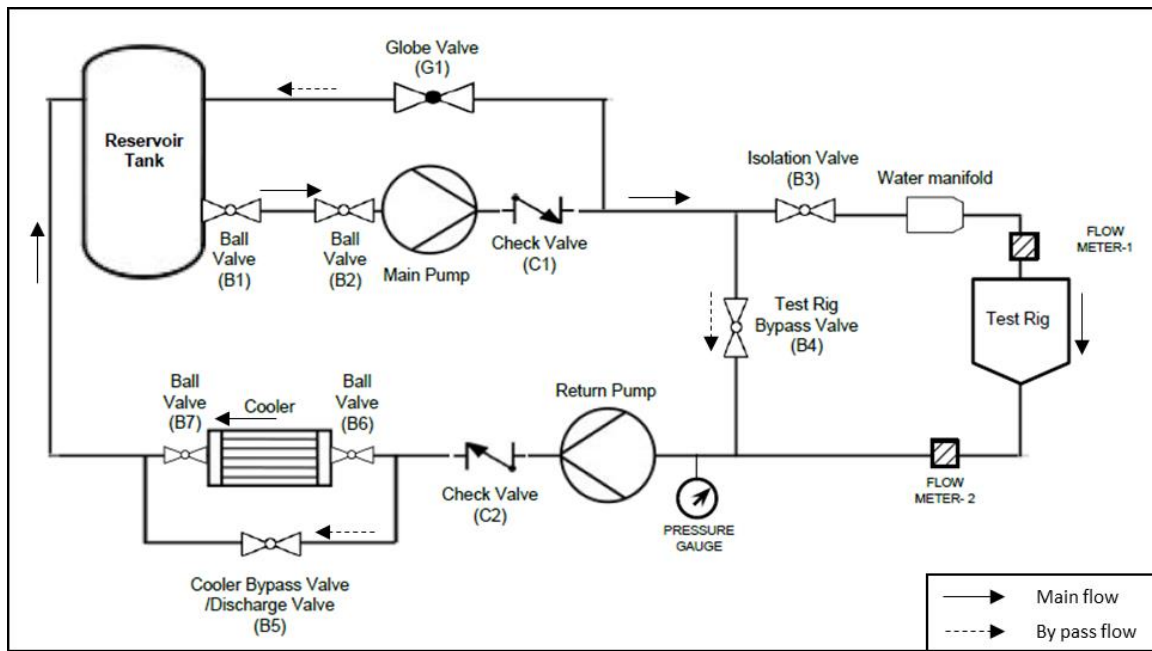


Figure 11: Schematic diagram of closed loop water supply system for thrust bearing test-rig [3]

Water loop is opening the ball valves, B1 and B2, which opens flow from reservoir tank to the main pump. All the valves in the main flow are opened up to the return pump. Once the water reaches the test rig, visible by slow leakage from the test thrust bearing, the main pump and the return pump is switched on. Initially, high leakage flow rate is observed at the test thrust bearing. Slight amount of static load (20 ~ 30 lb.) is applied to control the leakage and balance the water loop. Water loop is considered balanced when there is no leakage from the thrust bearings.

Both the radial tilting pad bearings operate at a supply pressure of 50 psi. Supply pressure at the test thrust bearing and slave thrust bearing is adjusted according to operating conditions. Since they react to applied load as a pair, the pressure in thrust bearings is always same. Once the pressures are set, desired static load is achieved by adjusting the load application cable. The leakage is monitored each time after adjusting the loads to ensure if the loop is balanced. Globe Valve, G1, is used to adjust the flowrate from the main

pump to balance the water loop. The water loop is usually balanced in 2 to 3 iterations.

Motor Startup and Operation

The motor connected to the rotor in the thrust bearing test rig is controlled by a Variable Frequency Drive (VFD). Before startup, a pre-startup inspection is conducted to ensure if the rotor is rotating smoothly. This step is conducted to avoid rubbing between rotor and radial bearings at high speeds. It involves rotating the rotor by hand to gage resistance in rotation. Also, the eddy current sensor readings in the Alignment LabVIEW program is used to monitor the clearance between the runner and the rotor to ensure there is sufficient clearance between the Test TB and the runner. As a standard practice, clearance from all eddy current probes should be above 35 μm to clear pre-startup inspection.

Once the pre-startup inspection is complete, the VFD is switched on along with its cooling system. The speed is increased in steps of 500 RPM until the desired speed is achieved. At each step, the clearance from the proximity probes of the test thrust bearing is monitored to ensure safe operations. The motor is taken up to desired speed and operated for 3 mins before readings are taken.

Once the rig startup procedure is complete, measurements are recorded based on the type of load applied on the test thrust bearing.

Static Load Measurements

Static load is applied through the cable and measured through the static load cell. A LabVIEW VI used to take static measurements at different test parameters. This VI measures the following parameters

- Clearance between test thrust bearing and runner from eddy current sensors for test thrust bearing
- Clearance between slave thrust bearing and runner from eddy current sensors for slave thrust bearing
- Exhaust flow rate at test thrust bearing
- Inlet flow rate at test thrust bearing
- Pressure at land of test thrust bearing

Impact Load Measurements

Prior to initiating shaft rotation, pressurized water supplies the journal bearings at 50 psi(g) and lifts the rotor. Water at 70 psi(g) supplies the slave and test thrust bearings. The static loading mechanism loads the test thrust bearing between 40 and 60 lbf. An alignment procedure ensures the test thrust bearing surface presses flush against the rotor thrust collar. Once aligned, a Variable Frequency Drive (VFD) controls an electric motor to ramp up to a specified rate, ranging from 3 krpm to 6krpm. An automatic impact hammer then delivers a dynamic load axially to the load shaft and the dynamic response of the test thrust bearing is measured.

An accelerometer mounted directly to the test thrust bearing housing measures acceleration in the axial direction, three proximity sensors enable the clearance to be determined at the center of the test thrust bearing and a load cell mounted in series with the load shaft measures tension and compression forces. For each test condition, 100 total impacts are recorded, each consisting of 16,386 samples recorded at a rate of 31,250 Hz. Time response data is converted into the frequency domain using the Fast Fourier Transform (FFT) algorithm in Matlab at which point they are averaged. The frequency response data is applied to the derived impedance function (H), where the curve-fit of the real and imaginary plots reveal the force parameters of the test thrust bearing (stiffness, damping and added mass).

Thrust Bearing Dynamic Performance for Tests with Moderate Rotor Speed

Figure 12 shows an example of curve fits of the real and imaginary plots of the impedance function used to determine the test thrust bearing force coefficients for an impact test with 3krpm shaft rotational speed, 70 psi(g) thrust bearing supply pressure and 40 lbf applied static load. The real part is plotted against the frequency squared ($(\text{rad/s})^2$) and fitted with a linear line. The slope of this line represents the added mass coefficient (kg) and the intersection with the y-axis represents the stiffness (N/m). The imaginary part of the impedance function is plotted against the frequency (rad/s) and fitted with a linear line with intercept at the origin. The slope of this line represents the derived damping of the test thrust bearing.

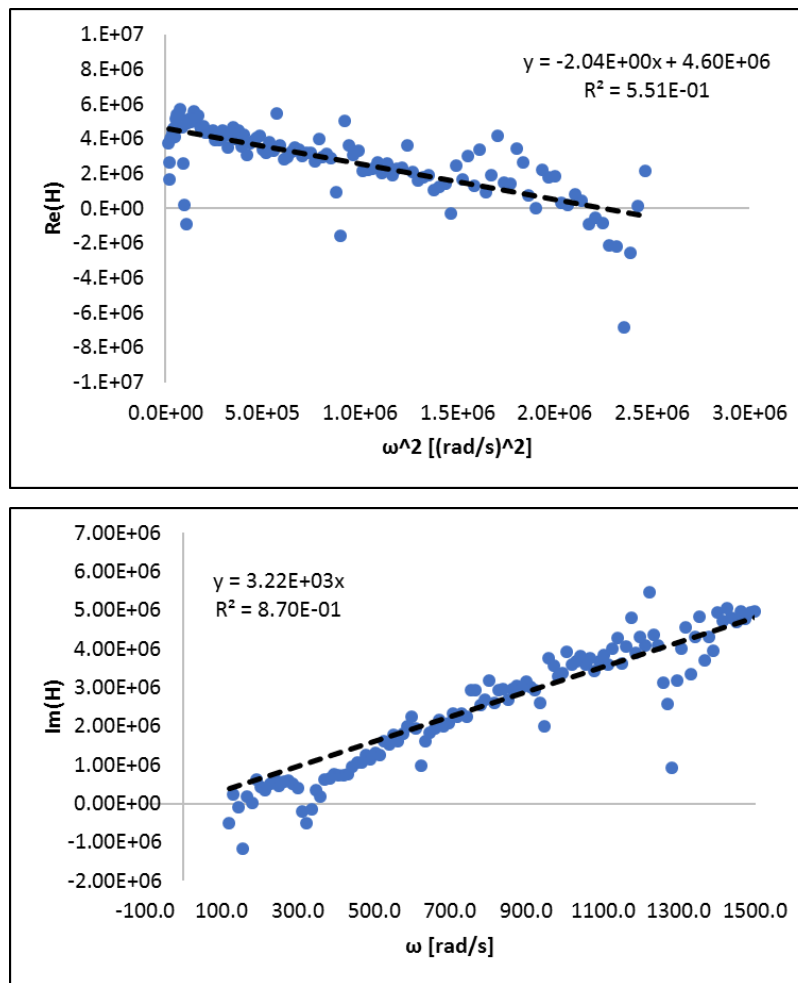


Figure 12. Example of the curve fitting procedure used to determine the force coefficients of the water lubricated test thrust bearing from the derived impedance function. The top plot represents the real part of impedance with respect to frequency squared ($(\text{rad/s})^2$) where the stiffness and added mass are identified as intersection with the y-axis and the slope of the linear curve fit, respectively. The bottom plot represents the imaginary part of the impedance function with respect to frequency (rad/s) where the slope of the linear curve fit with intercept through the origin representing the identified damping of the system.

Variable Rotor Speed

Figure 13 shows predicted and measured stiffness (N/m) with respect to increasing rotor speed for the test thrust bearing subjected to three applied static loads, 40, 50 and 60 lbf and 70 psi(g) thrust bearing supply pressure. As expected, when static load increases, bearing stiffness also increases. As rotor speed increases, however, bearing stiffness does not change appreciably. Both measurements and predictions capture this behavior. This indicates that the test thrust bearing performs primarily as a hydrostatic bearing for the range of operating speeds examined herein.

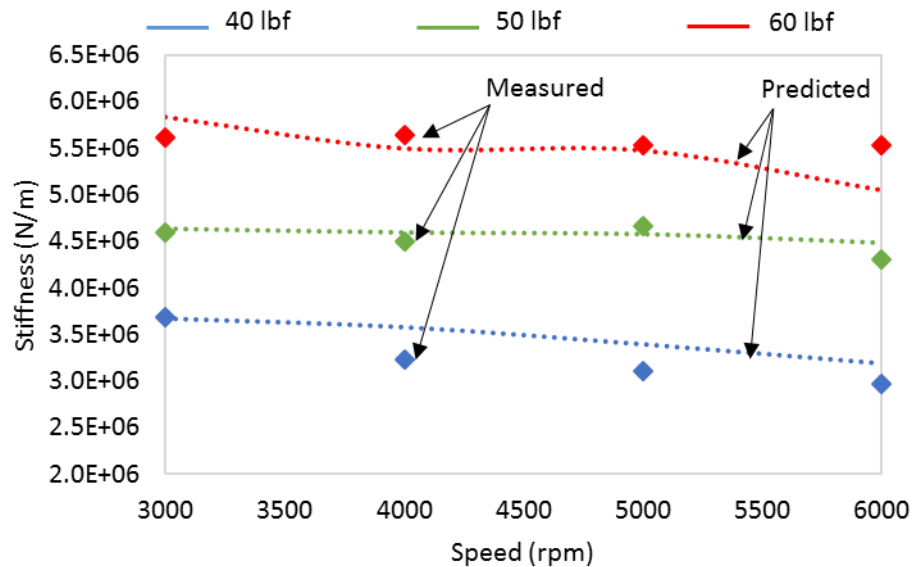


Figure 13. Predicted and measured thrust bearing stiffness (N/m) for the test thrust bearing operating with water supplied at 70 psi(g) and shaft rotational speed of 3 krpm, 4krpm, 5krpm and 6krpm. Journal bearings supplied with water at 50 psi(g) support the rotor. The frequency range used for identification is 0-250 Hz based on coherence. 100 impact tests, each consisting of 16,386 samples recorded with a sampling frequency of 31,250 Hz, are averaged.

Figure 14 shows predicted and measured damping (Ns/m) with respect to increasing rotor speed for the test thrust bearing subjected to three applied static loads, 40, 50 and 60 lbf and 70 psi(g) thrust bearing supply pressure. Both predictions and measured results indicate minimal change in thrust bearing damping characteristic with increase in rotor speed with a damping increase with increasing static load. Although measured damping magnitude exceeds the predicted values for the 60 lbf applied load cases, the magnitude of predictions and measurements agree well and further validate that the thrust bearing does not exhibit appreciable hydrodynamic behavior for the aforementioned test conditions.

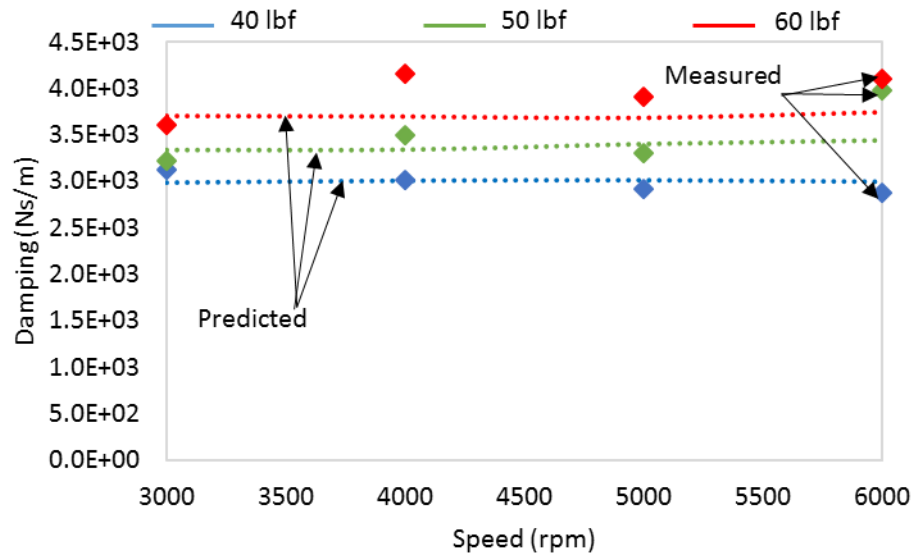


Figure 14. Predicted and measured thrust bearing damping (Ns/m) for the test thrust bearing operating with water supplied at 70 psi(g) and shaft rotational speed of 3 krpm, 4krpm, 5krpm and 6krpm. Journal bearings supplied with water at 50 psi(g) support the rotor. The frequency range used for identification is 0-250 Hz based on coherence. 100 impact tests, each consisting of 16,386 samples recorded with a sampling frequency of 31,250 Hz, are averaged.

Figure 15 shows the measured added mass (kg) with respect to increasing rotor speed for the test thrust bearing subjected to three applied static loads, 40, 50 and 60 lbf and 70 psi(g) thrust bearing supply pressure. Predictions show no significant change in added mass with change in shaft speed or applied. Measured results qualitatively agree with the predicted minimal change with increasing rotor speed. However, the magnitude of the measured values exceed the predicted values and indicate an increase with increasing applied static load. High amplitude measured added mass values can be attributed to friction losses incurred during impact that are not accounted for in the predictive software. These losses, although minimized as much as possible during the testing process, may be attributed to load shaft rub against equipment housing due to load shaft misalignment and/or worn aerostatic load shaft radial support bearings. These friction losses would be exacerbated with increasing static load which would explain the net increase in added mass with respect to static load seen in Figure 15.

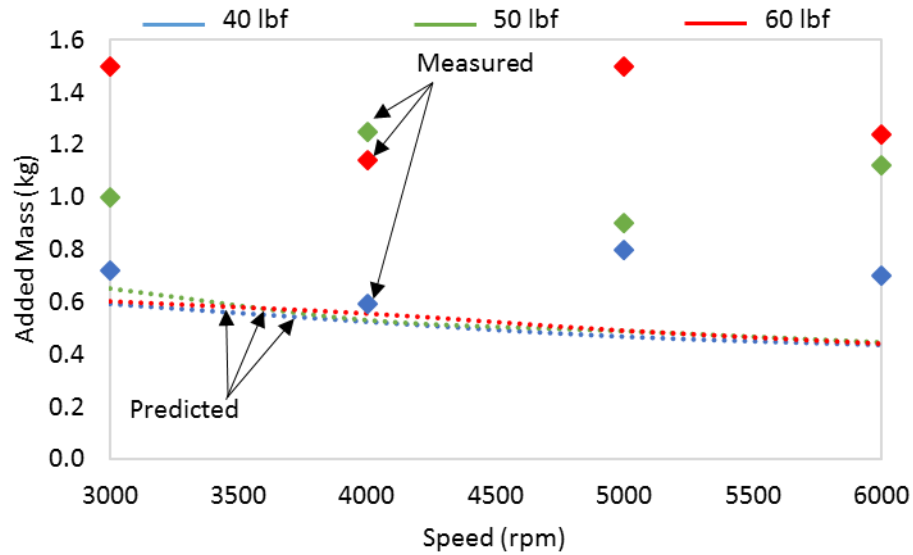


Figure 15. Predicted and measured thrust bearing added mass (kg) for the test thrust bearing operating with water supplied at 70 psi(g) and shaft rotational speed of 3 krpm, 4krpm, 5krpm and 6krpm. Journal bearings supplied with water at 50 psi(g) support the rotor. The frequency range used for identification is 0-250 Hz based on coherence. 100 impact tests, each consisting of 16,386 samples recorded with a sampling frequency of 31,250 Hz, are averaged.

Variable Thrust Bearing Supply Pressure

Figure 16 shows the measured thrust bearing stiffness (N/m) with respect to increasing thrust bearing supply pressure and constant 3krpm rotational speed. With increasing supply pressure, measured stiffness increases. This behavior correlates well with the predicted stiffness behavior although the rate of increase is predicted to be higher than what was measured.

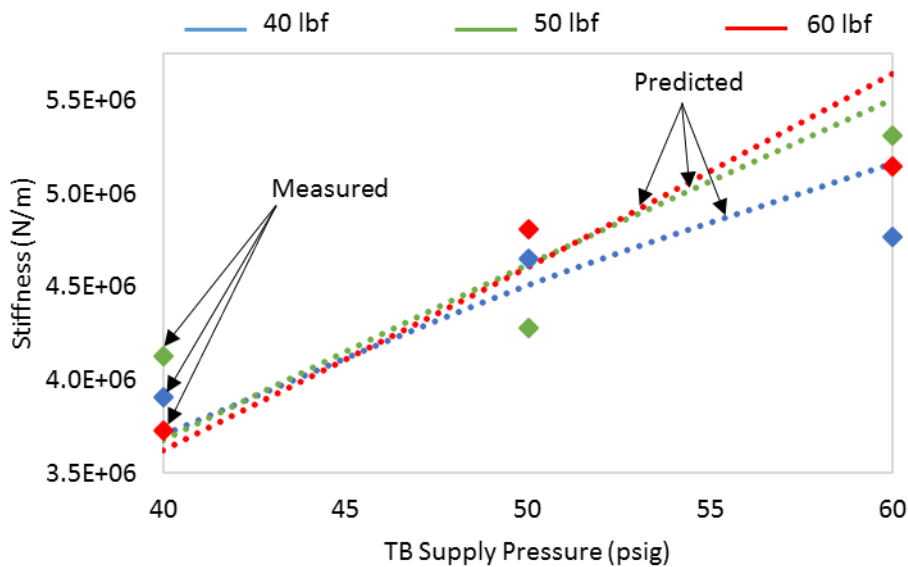


Figure 16. Predicted and measured thrust bearing stiffness (N/m) for the test thrust bearing operating with water supplied at 40, 50 and 60 psi(g) and shaft rotational speed of 3 krpm. Journal bearings

supplied with water at 50 psi(g) support the rotor. The frequency range used for identification is 0-250 Hz based on coherence. 100 impact tests, each consisting of 16,386 samples recorded with a sampling frequency of 31,250 Hz, are averaged.

Figure 17 shows the measured damping (Ns/m) with respect to increasing thrust bearing supply pressure and constant 3krpm rotational speed. As seen with the predicted stiffness behavior, damping is also predicted to increase with increasing supply pressure. The magnitude of the measured damping values exceeds predictions for all but the 60 psi(g), 40 lbf test condition although the rate of damping increase closely matches the predicted rate, especially for 40 and 50 lbf applied static load.

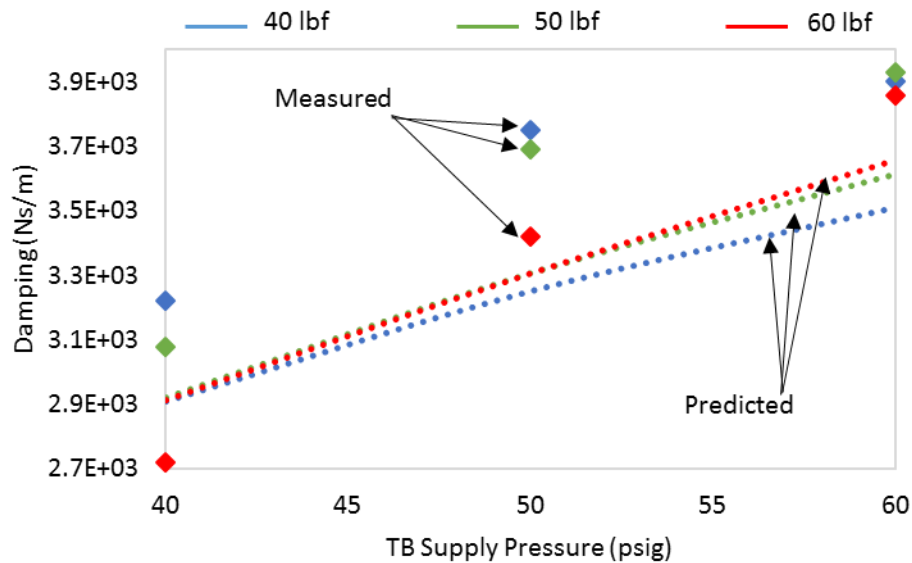


Figure 17. Predicted and measured thrust bearing damping (Ns/m) for the test thrust bearing operating with water supplied at 40, 50 and 60 psi(g) and shaft rotational speed of 3 krpm. Journal bearings supplied with water at 50 psi(g) support the rotor. The frequency range used for identification is 0-250 Hz based on coherence. 100 impact tests, each consisting of 16,386 samples recorded with a sampling frequency of 31,250 Hz, are averaged.

Figure 18 shows the measured added mass (kg) with respect to increasing thrust bearing supply pressure and constant 3krpm rotational speed. As seen with the added mass with respect to increasing rotational speed presented in Figure 15, the measured added mass coefficient exceeds the predicted value for all cases. Both predictions and measurements indicate minimal change in magnitude with increase in bearing supply pressure. High measured added mass measurements may be attributed to frictional losses within the system.

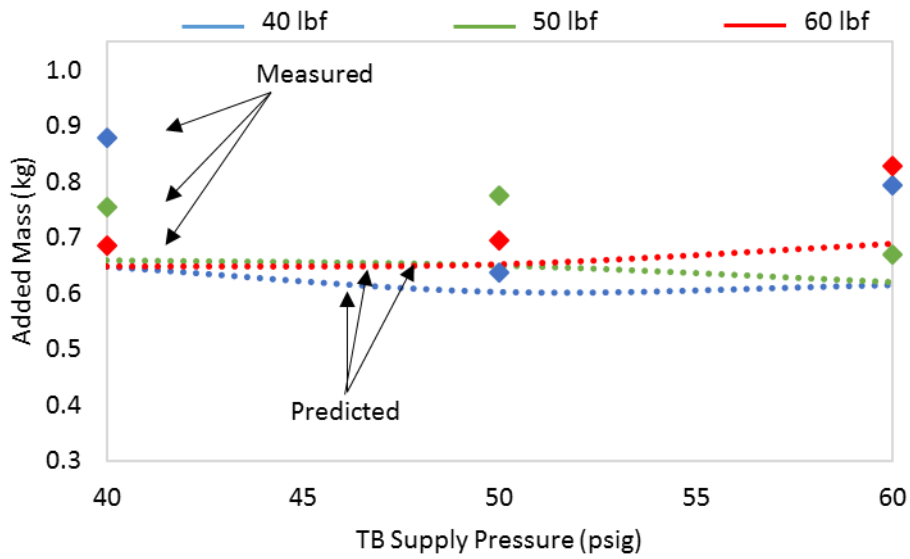


Figure 18. Predicted and measured thrust bearing added mass (kg) for the test thrust bearing operating with water supplied at 40, 50 and 60 psi(g) and shaft rotational speed of 3 krpm. Journal bearings supplied with water at 50 psi(g) support the rotor. The frequency range used for identification is 0-250 Hz based on coherence. 100 impact tests, each consisting of 16,386 samples recorded with a sampling frequency of 31,250 Hz, are averaged.

Conclusion

For operation with moderate shaft speed (up to 6krpm), dynamic behavior of a water lubricated thrust bearing is measured through impact testing and quantified with force coefficients derived from the system impedance function. Measurements indicate that the test thrust bearing shows no appreciable change in dynamic characteristic with change in rotor speed. This behavior is understandable due to the lack of hydrodynamic features on the bearing surface such as tapered sections or tilting pads. In short, the bearing behaves as a purely hydrostatic bearing for the range of rotor speeds examined herein. With increase in applied static load, however, bearing stiffness and damping increase while added mass does not show appreciable change. Measured bearing dynamic behavior with increasing static load correspond well to predicted values. With constant supply pressure, increase in applied load leads to a decrease in clearance between the thrust bearing face and the rotor thrust collar which, in turn, leads to an increase in stiffness and damping due to the increase in flow resistance. Discrepancies between predicted and measured added mass coefficients can be attributed to friction losses incurred during impact that are not accounted for in the predictive software. These losses, although minimized as much as possible during the testing process, may be attributed to load shaft rub against equipment housing due to load shaft misalignment and/or worn aerostatic load shaft radial support bearings.

Additionally, Appendix D details the design of a fixed geometry hydrodynamic thrust bearing which has since been fabricated. Future work will consist of installing and testing this bearing with the current test rig at speeds up to 9 krpm.

References

- [1] San Andrés, L., 2010, “Modern Lubrication Theory, One Dimensional Fluid Film Bearings,” Notes 2-Appendix, Texas A&M University Digital Libraries, <http://hdl.handle.net/1969.1/93254> [5 April 2016].
- [2] San Andrés, L., 2013, “A Test Rig for Evaluation of Thrust Bearings and Face Seals,” Proposal to the Turbomachinery Research Consortium, Turbomachinery Laboratory, Texas A&M University, College Station, TX.
- [3] M. Rohmer, L. San Andres, S. Wilkinson, and H. Jani, 2016, “Measurement of Static Load Performance in a Water Lubricated Hybrid Thrust Bearing,” Annual Progress Report to the Turbomachinery Research Consortium, TRC-B&C-03-2016, Turbomachinery Laboratory, Texas A&M University, College Station, TX.
- [4] Esser, P., 2010, “Measurements versus Predictions for a Hybrid (Hydrostatic plus Hydrodynamic) Thrust Bearing for a Range of Orifice Diameters,” M.S. Thesis, Mechanical Engineering, Texas A&M University.
- [5] Rohmer, M., Wilkinson, S. and San Andrés, L., 2015, “Revamping and Preliminary Operation of a Thrust Bearing Test Rig,” Annual Progress Report to the Turbomachinery Research Consortium, TRC-B&C-03-2015, Turbomachinery Laboratory, Texas A&M University, College Station, TX.
- [6] Forsberg, M., 2008, “Comparison between Predictions and Experimental Measurements for an Eight Pocket Annular HTB,” M.S. Thesis, Mechanical Engineering, Texas A&M University, College Station, TX.
- [7] Dadouche, A., Fillon, M., and Dmochowski, W., 2006, “Performance of a Hydrodynamic Fixed Geometry Thrust Bearing: Comparison between Experimental Data and Numerical Results,” *Tribology Transactions*, **49**(3), pp. 419-426.
- [8] Wasilczuk, M., 2015, "Friction and Lubrication of Large Tilting-Pad Thrust Bearings", *Lubricants*, **3**(2), pp. 164-180.

- [9] San Andrés, L., 2010, "Modern Lubrication Theory, Introduction to Hydrodynamic Bearings," Notes 1, Texas A&M University Digital Libraries, <http://hdl.handle.net/1969.1/93254> [5 April 2016].
- [10] Frêne, J., 1997, Hydrodynamic lubrication, Elsevier, Amsterdam.
- [11] 2017, "Hydrodynamic Lubrication", Marinediesels.info [Online]. Available: http://www.marinediesels.info/2_stroke_engine_parts/Other_info/hydrodynamic_lubrication.htm. [Accessed: 26- Mar- 2017].
- [12] Pinkus, O., and Sternlicht, B., 1989, Theory of hydrodynamic lubrication, University Microfilms, Ann Arbor, Mich.
- [13] 1996, "Thrust Bearing Analysis, Optimization and Case Histories", 25th Turbomachinery Research Symposium, Turbomachinery Laboratory, Texas A & M University, pp. 17-24.
- [14] Gohar, R., and Advani, S., 1973, "A simplified design method for taper-land thrust bearings", Tribology, **6**(2), pp. 50-56.
- [15] Frene, J., 1978, "Tapered Land Thrust Bearing Operating in Both Laminar and Turbulent Regimes", A S L E Transactions, **21**(3), pp. 243-249.
- [16] Pinkus, O., 1981, "Centrifugal Effects in Thrust Bearings and Seals under Laminar Conditions", Journal of Tribology, **103**(1), p. 126.
- [17] Hashimoto, H., 1989, "The Effects of Fluid Inertia Forces on the Static Characteristics of Sector-Shaped, High-Speed Thrust Bearings in Turbulent Flow Regime", Journal of Tribology, **111**(3), p. 406.
- [18] Henry, Y., Bouyer, J., and Fillon, M., 2014, "An Experimental Hydrodynamic Thrust Bearing Device and Its Application to the Study of a Tapered-Land Thrust Bearing", Journal of Tribology, **136**(2), p. 021703.
- [19] Song, Y., Ren, X., Gu, C., and Li, X., 2014, "Experimental and Numerical Studies of Cavitation Effects in a Tapered Land Thrust Bearing", Journal of Tribology, **137**(1), p. 011701.

- [20] Ramirez, F., 2008, "Comparison between Predictions and Measurements of Performance Characteristics for an Eight Pocket Hybrid (Combination Hydrostatic/Hydrodynamic) Thrust Bearing," M.S. Thesis, Mechanical Engineering, Texas A&M University.
- [21] Gardner, W. W., 1975, "Performance Tests on Six-Inch Tilting Pad Thrust Bearings." *Journal of Lubrication Technology*, **97** (3), pp 430-438.
- [22] Glavatskih, S. B. 2002. "Laboratory Facility for Testing Hydrodynamic Thrust Bearings." *Journal of Engineering Tribology*, **216** (2), pp 1-12
- [23] 2017, "Wedge action and the thrust pad", Ivorbittle.co.uk [Online]. Available: <http://www.ivorbittle.co.uk/Books/Fluids%20book/Chapter%2016%20web%20docs/Wedge%20action%20and%20the%20thrust%20pad.htm>. [Accessed: 24- Mar- 2017].
- [24] Constantinescu, V.N., 1959, "On Turbulent Lubrication", *Proceedings of the Institution of Mechanical Engineering*, London, **38**, 1959, pp 28-46.

Appendix A: Predictive Codes for Bearing Performance

XLHydroJet® and XLHydroThrust® predict the static load performance and force coefficients for hydrostatic journal bearings and hydrostatic thrust bearings, respectively. Tables and show the required inputs and the outputs for XLHydroJet® [A3] and XLHydroThrust® [A1], respectively. XLTRC2® [A2], a rotordynamic suite, is used to produce predictions for a rotordynamic system, such as natural frequency, damping ratio, and imbalance response.

Table 3: XLHydroJet Inputs and Outputs

Inputs	Outputs
Bearing Geometry	Stiffness (Direct and Cross-Coupled)
Pad Geometry	Damping (Direct and Cross-Coupled)
Pocket Geometry	Added Mass (Direct and Cross-Coupled)
Orifice Geometry	Impedances (Direct and Cross-Coupled)
Lubricant Properties	Static Eccentricity
Thermal Options	Mass Flow Rate
Supply Pressure	Static Reaction Force
Exit Pressure	Power Loss
Rotor Speed	Equivalent Stiffness
Excitation Frequency	Whirl Frequency Ratio
Static Load/Static Eccentricity	Drag Torque
Fluid Inertia Presence	Maximum Pressure
Mesh Size	Maximum Temperature

Table 4: XLHydroThrust Inputs and Outputs

Inputs	Outputs
Bearing Geometry	Force and Moment Stiffness (Direct)
Bearing Misalignment	Force and Moment Stiffness (Cross
Lubricant Properties	Coupled)
Maximum Iterations	Force and Moment Damping (Direct)
Mesh Size	Force and Moment Damping (Cross
Roughness Factors	Coupled)
Rotor Speed	Force and Moment Added Mass (Direct)
Thermal Options	Force and Moment Mass (Cross Coupled)
Pad Geometry	Clearance
Supply Pressure	Mass Flow Rate at Inner Diameter
Exit Pressure	Mass Flow Rate at Outer Diameter
Initial Clearance	Static Reaction Force
Static Load	Power Loss
Fluid Inertia Presence	Maximum Pressure
Units	Maximum Temperature

References

- [A1] San Andrés, L., 2002, "Effects of Misalignment on Turbulent Flow Hybrid Thrust Bearings," ASME J. of Trib., **124**(1), pp. 212-219.
- [A2] XLTRC2, 2002, Computational Rotordynamics Software Suite, Turbomachinery Laboratory, Texas A&M University, College Station, TX.
- [A3] San Andres, L., and Childs, D., 1997, "Angled Injection—Hydrostatic Bearings Analysis and Comparison to Test Results", Journal of Tribology, **119**(1), p. 179.

Appendix B: Identification of Thrust Bearing Force Coefficients [B1]

Thrust bearing force coefficients (stiffness K , damping C , and added mass M) enable the prediction and control of axial rotor motions under dynamic loading. Obtaining reliable estimates of the bearing operating performance in actual test conditions is (although challenging) necessary to reduce the discrepancy between measurements and predictions [B1].

Figure 19 shows a schematic view of the test thrust bearing and load shaft assembly modeled as a one degree of freedom (1-DOF) system¹. Let z_{TTB} and z_R be the absolute axial displacements of the TB and rotor, respectively, and $z = z_{TTB} - z_R$ is the relative displacement between both components. Additionally, a taut steel cable of stiffness K_{Cable} applies the static force to the load shaft. A simple longitudinal load vs. displacement experiment determines K_{Cable} . A linear viscous damper (C_{TTB}), stiffness (K_{TTB}), and mass (M_{TTB}) denote the action of the thrust fluid film bearing.

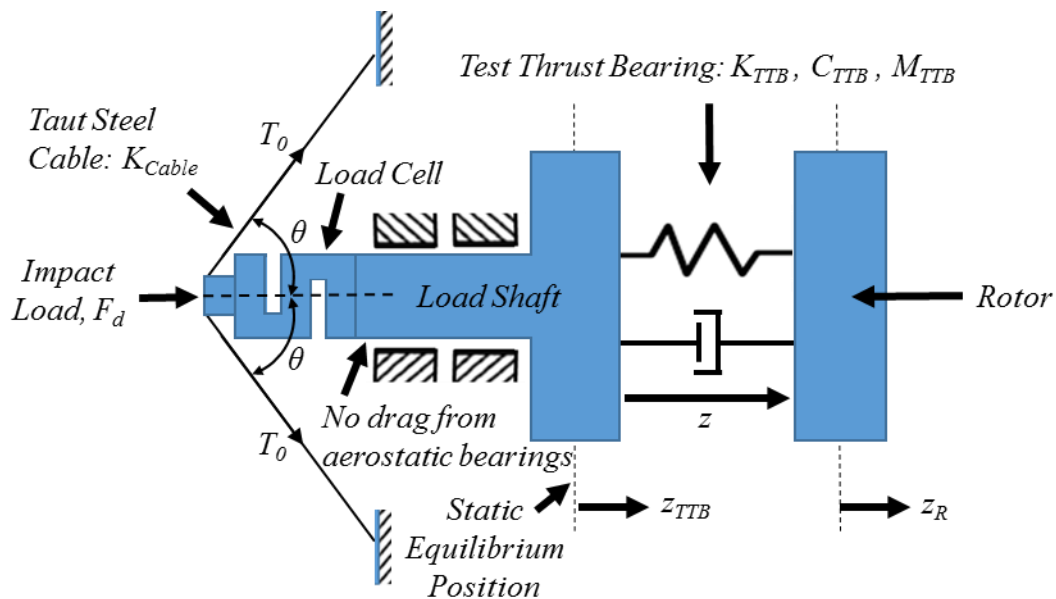


Figure 19: Schematic view of 1-DOF model of test TB for parameter identification.

The instrumentation used during the dynamic tests includes six eddy current sensors (three on each thrust bearing), one piezoelectric accelerometer affixed to the test thrust

¹ Model assumes no dynamic tilts or rotation

bearing cartridge along the axial direction, and one load cell mounted on one end of the static loader. Three eddy current sensors define a plane and enable calculation of the operating clearance at the center of the test TB and slave TB.

At static equilibrium, the applied load F_0 is balanced by the test TB force, F_{TB_0} , generated by equilibrium clearance $c_0 = z_0$.

Due to an impact load ($F_{d(t)}$), the test element (thrust bearing) undergoes small amplitude motions about its static equilibrium position. The test and slave thrust bearings react to the impact force. Eddy current sensors record the induced motion while an accelerometer fixed to the load shaft assembly measures its acceleration (\ddot{z}_{TTB}). Assuming no axial drag from the aerostatic bearings, the equation of motion (EOM) for the system undergoing axial motions is:

$$M\ddot{z}_{TTB} = F_{d(t)} + F_{Cable} - F_{TTB} \quad (B1)$$

where $F_{d(t)}$ is an applied impact load, F_{Cable} is the force exerted by the taut cable on the load shaft, and F_{TTB} is the TTB reaction force equal to $F_{TTB} = F_{TTB_0} + F_{TTB_d(t)}$.

Assuming a massless and undamped cable, the force exerted by the cable is:

$$F_{Cable} = 2T_0 \cos \theta - K_{Cable} z_{TTB} \quad (B2)$$

At equilibrium,
$$F_{TTB_0} = 2T_0 \cos \theta \quad (B3)$$

Represent the dynamic component of the TTB force as

$$F_{TTB_d(t)} \approx K_{TTB} z_{(t)} + C_{TTB} \dot{z}_{(t)} + M_{TTB} \ddot{z}_{(t)} \quad (B4)$$

where K_{TTB} , C_{TTB} , and M_{TTB} are the bearing axial force coefficients (stiffness, damping and added mass, respectively). Hence, Eq. (1) becomes

$$M\ddot{z}_{TTB} = F_{d(t)} - K_{Cable} z_{TTB} - K_{TTB} z_{(t)} - C_{TTB} \dot{z}_{(t)} - M_{TTB} \ddot{z}_{(t)} \quad (B5)$$

The discrete Fourier transform (DFT) algorithm transforms force, displacement and acceleration data from the time domain into the frequency domain. Let

$$\bar{z}_{(\omega)} = DFT(z_{(t)}), \bar{F}_{(\omega)} = DFT(F_{(t)}), \bar{A}_{(\omega)} = DFT(\ddot{z}_{TTB(t)}), \bar{z}_{TTB(\omega)} = DFT(z_{TTB(t)}) \quad (B6)$$

where ω denotes frequency. Recall that

$$i\omega\bar{z}_{(\omega)} = DFT(\dot{z}_{(t)}), \quad -\omega^2\bar{z}_{(\omega)} = DFT(\ddot{z}_{(t)}) \quad (\text{B7})$$

where $i = \sqrt{-1}$ is the imaginary unit. Hence, in the frequency domain Eq. (5) becomes

$$H_{(\omega)} = \frac{\bar{F}_{d(\omega)} + (K_{Cable}/\omega^2 - M)\bar{A}_{(\omega)}}{\bar{z}_{(\omega)}} = K_{TTB} - M_{TTB}\omega^2 + i\omega C_{TTB} \quad (\text{B8})$$

Where H is the dynamic (complex) stiffness for the test element. With $H_{(\omega)}$ obtained, the estimation of the TB axial force coefficients follows from curve fitting of the real and imaginary parts of the complex stiffness, i.e.

$$Re(H_{(\omega)}) \rightarrow (K - M\omega^2)_{TTB}, \quad Im(H_{(\omega)}) \rightarrow C_{TTB}\omega \quad (\text{B9})$$

Note M = 1.6094 kg based on scale measurements which includes the mass of the load shaft, TB and load cell.

References

- [B1] Tiwari, R., Lees, A. W., and Friswell, M. I., 2004, “Identification of Dynamic Bearing Parameters: A Review,” *Shock Vib. Dig.*, **36**, pp. 99–124.
- [B2] San Andrés, L., 2014, “Mechanical Vibrations, Numerical solution of EOM for a Single Degree of Freedom (SDOF) system,” Notes 6, Texas A&M University Digital Libraries, <http://hdl.handle.net/1969.1/93271> [5 April 2016].
- [B3] San Andrés, L., 2010, “Modern Lubrication Theory, Experimental Identification of Bearing Force Coefficients,” Notes 14, Texas A&M University Digital Libraries, <http://hdl.handle.net/1969.1/93254> [5 April 2016].
- [B4] Wilkinson, M., 2016, *Static and Dynamic Load Performance of a Water Lubricated Hybrid Thrust Bearing: Measurements and Validation of a Predictive Tool*, College Station, TX,

Appendix C: Thrust Collar Plane Equation Derivation [C1]

Eddy current sensors face a thrust collar and measure the axial gap between the thrust collar and TB surface at three circumferential locations, as shown in Figure 7. Using the gap clearances and the geometry to determine the clearance between the thrust collar and the TB surface at the center of the TB and the tilt of the thrust collar relative to the TB is critical in order to estimate the TB performance.

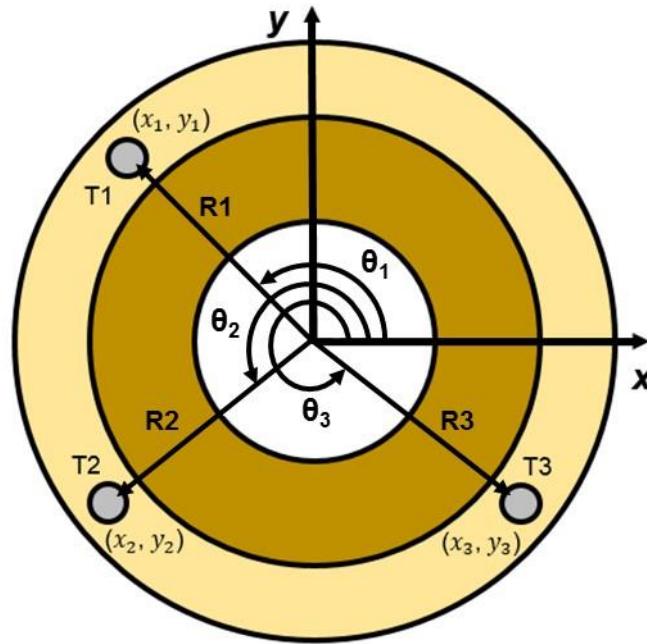


Figure 20: Reference diagram of a thrust bearing for geometric calculation for Location of Proximity Probes

Table 9 describes the horizontal and vertical position of each eddy current sensor relative to the center of the TB.

Table 9. Horizontal and vertical positions of each eddy current sensor relative to the center of the thrust bearing.

	X	y
Probe T1	$x_1 = -33.02 \text{ mm}$	$y_1 = 27.69 \text{ mm}$
Probe T2	$x_2 = -37.34 \text{ mm}$	$y_2 = -21.59 \text{ mm}$
Probe T3	$x_3 = 37.34 \text{ mm}$	$y_3 = -21.59 \text{ mm}$

Assuming the TB and the thrust collar act as rigid planes, the gap between the thrust collar and the TB surface at each eddy current sensor can be used with the position of each

eddy current sensor to determine the equation of the plane of the rotor thrust collar relative to the TB. To derive the rotor thrust collar plane equation, first establish a vector to define the distance from the TB center to each sensor and the angle between each vector and the x-axis as,

$$R_i = \sqrt{y_i^2 + x_i^2} \quad , \quad \theta_i = \tan^{-1}(y_i/x_i) \quad (C1)$$

Respectively.

The axial gap at the center of the TB (C_0) as well as the tilt of the rotor thrust collar about the x-axis (δ_x) and y-axis (δ_y) relative to the TB define the clearance at any point on the thrust collar surface (C_i),

$$C_i = C_0 + R_i \cos \theta_i \delta_y + R_i \sin \theta_i \delta_x \quad (C2)$$

which can be simplified to the following form,

$$C_i = C_0 + X_{Si} \delta_y + Y_{Si} \delta_x \quad (C3)$$

The transformation matrix,

$$A_T = \begin{bmatrix} 1 & X_{S1} & Y_{S1} \\ 1 & X_{S2} & Y_{S2} \\ 1 & X_{S3} & Y_{S3} \end{bmatrix} \quad (C4)$$

enables the conversion of the axial clearance measurements from each sensor (C_1 , C_2 , and C_3) into C_0 , δ_y and δ_x with the following relation,

$$\begin{bmatrix} C_0 \\ \delta_y \\ \delta_x \end{bmatrix} = A_T \begin{bmatrix} C_1 \\ C_2 \\ C_3 \end{bmatrix}$$

REFERENCES

- [C1] Forsberg, M., 2008, "Comparison between Predictions and Experimental Measurements for an Eight Pocket Annular HTB," M.S. Thesis, Mechanical Engineering, Texas A&M University, College Station, TX..

Appendix D: Hydrodynamic Thrust Bearing Design

Testing the hydrodynamic thrust bearing and comparing the experimental results is the next stage in the research to further validate the XLHydroThrust® code. For this purpose, a hydrodynamic bearing is designed for the thrust bearing test rig.

The first step in the design process is to select the type of hydrodynamic bearing. It requires theoretical analysis and judgement on factors like space limitations and design complexity. Among thrust bearings, as discussed earlier in the report, tapered land bearings have advantages over tilting pad thrust bearing which includes ease of manufacturing. Therefore, a fixed geometry tapered land thrust bearing is an ideal choice. Also, the literature available on axial response of tapered land thrust bearings is limited. Because most industrial equipment operates at fixed speed during regular operations, tapered land thrust bearing experimental validation of a predictive tool will have a significant impact.

Hydrodynamic Thrust Bearing Material

The material selection for the hydrodynamic bearing is made based on its compatibility with the lubricant, in this case, water. Corrosion resistant alloys are required for bearing surfaces and structural components. Due to lower viscosity as compared to oil, water bearings have lower film thickness [E2]. This warrants a need for protective layer of noncorrosive material over the bearing. The material also should have exceptionally low friction even under dry conditions.

Based on these criteria, the material selected for thrust bearings is a stainless steel with a Polyether Ether Ketone (PEEK) polymer coating. PEEK is an engineering polymer with many advantages such as lightweight, high thermal stability, high strength coupled with toughness [E3]. Load support is linearly related to rotor speed, making these hydrodynamic bearings vulnerable to rubbing during start up and shut down. The PEEK coating acts as a protective layer during these low rotor speed conditions. For this application of the thrust bearing, between the coating and the bearing, there is a bronze sintered layer. The steel backing is bonded to the porous bronze sintered layer and it provides a strong mechanical bond between the backing and the PEEK Coating.

Bearing Design Calculations

With the selection of a fixed geometry as the bearing type, bearing features are optimized to perform within the operating conditions of the test rig. . Figure 21 shows an example of a tapered land thrust bearing design.

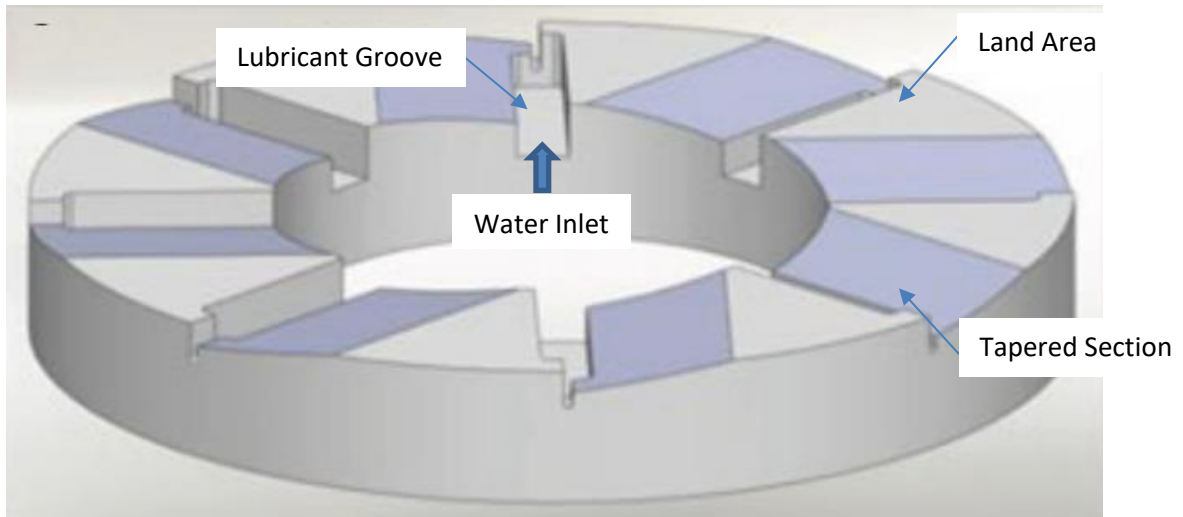


Figure 21: Fixed Geometry Tapered Land Thrust Bearing [E6]

For these features, bearing design calculations determine the taper features, pad length, lubricant groove and feed holes. Additional features enable the bearing to be compatible with the test rig and all required instrumentation.

For bearing calculations, a plane slider bearing configuration is considered, as is depicted in Figure 22.

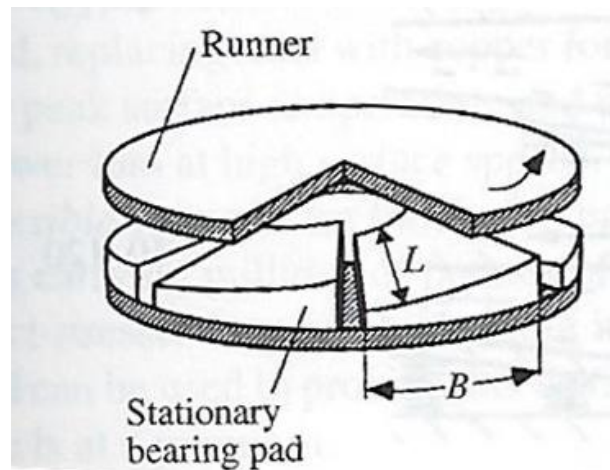


Figure 22: Thrust Bearing and Runner (E12)

Thrust bearing design pursued here is based on maximum load capacity. Maximum Loads required for testing bearings according to TRC proposal is 150 lb. maintaining a factor of safety of 3, the bearings are design at 450 lb.

Design conditions for the thrust bearing was based on the following parameters

Table 5: Design Parameters for thrust bearings

Design Parameters
Inner Diameter – 0.8 inch
Maximum Speed – 9000 RPM
Outer Diameter – 1.5 inches
Maximum Load – 450 lb.

To study the hydrodynamic pressure generated by the bearing, Reynolds equation in cylindrical coordinate system is utilized [E12].

$$\frac{\partial}{\partial r} \left(\frac{\rho r h^3}{12\mu} \frac{\partial P}{\partial \theta} \right) + \frac{1}{r} \frac{\partial}{\partial \theta} \left(\frac{\rho h^3}{12\mu} \frac{\partial P}{\partial \theta} \right) = U \frac{\partial(\rho h)}{\partial \theta} - 12r\rho V_s \quad (E1)$$

For fixed geometry sectors such as tapered lands, a minimum film thickness is selected. This establishes a clearance h at center of each grid and its derivatives in the radial and circumferential directions. After the pressure distribution is obtained by a numerical procedure, total thrust load, power loss, and flow characteristics follow. To obtain these operating characteristics for a given applied load, this analytical routine is repeated while adjusting the minimum film thickness in a stepwise procedure until the calculated thrust load matches the given applied load.

Khonsari and Booser (2001) [E12] provide dimensionless force coefficients (K_h , K_f , K_q , K_s) obtained from the solution of constant viscosity Reynolds equation for tapered surface rectangular bearing segment. Table 6 shows coefficients for h_1/h_2 .

Table 6: Section from Table of Performance Coefficients for Tapered-Land Thrust Bearings [E12]

L/B	0.25	0.5	0.75	1	1.5	2	∞
$h_1/h_2 = 1.2$							
K_h	0.064	0.115	0.153	0.18	0.209	0.225	0.266
K_f	0.912	0.913	0.914	0.915	0.916	0.917	0.919
K_q	0.593	0.586	0.579	0.574	0.567	0.562	0.549
K_s	0.087	0.074	0.061	0.05	0.034	0.026	0

The solution covers wide range of aspect ratios along with a wide range of inlet to outlet film thickness ratios. These coefficients are used to calculate bearing characteristics using the following equations

Using a design load of 450 lb. and inner radius R_1 known from shaft diameter outer radius of the bearing is calculated using eq.

$$R_2 = \left(\frac{R_1^2 + W}{\pi k_g P} \right) \quad (E2)$$

Where

R_2 = Outer Radius (in.)

R_1 = Inner Radius (in.)

W = Applied load (lb.)

k_g = fraction of area between R_1 and R_2 not used for feed grooves = 0.85

P = Unit load (psi)

Using the value obtained for R_2 , mean radius R , radial length L and surface speed U is calculated from following equation. 15% of the total arc extent is dedicated to lubricant feed grooves. This factor is incorporated in the pad size using k_g . Total circumference for all the pads is calculated excluding the lubricant feed grooves Number of pads for the load is calculated by considering the pads as square shaped i.e. $B=L$

The value calculated for number of pads is approximated to whole, usually even, values for ease of machining. Once, the number of pads are found, taper on each pad is calculated using formula define by Wilcock and Booser (1957)

$$(h_1 - h_2) \approx 0.003B^{0.5} \quad (E3)$$

Next step is to assume minimum film thickness, h_2 and calculate h_1 using eq. (E3). Ratios of h_1/h_2 and L/B is used to obtain values from table 6 for dimensionless coefficients.

Using values of K_h and equation (E4), h_2 is computed.

$$h_2 = K_h \left(\frac{\mu UB}{P_{avg}} \right)^{0.5} \quad (E4)$$

This assumed film thickness is then adjusted in subsequent iterations until the calculated film thickness match assumed values.

Dimensionless coefficients (K_f , K_q , K_s) and equations (E5, E6, and E7) are used to calculate power loss, inlet flow rate, side leakage flow rate, respectively.

$$E_p = \frac{K_f \mu U^2 BL}{h_2} \quad (E5)$$

$$Q_1 = K_q ULh_2 \quad (E6)$$

$$Q_s = K_s ULh_2 \quad (E7)$$

Taper section of the pad is 51% of the total pad area. This selection is based on taper land bearing design in previous literature. Song, Y et al. (2014) use taper section which is 55% of total pad area for tapered land thrust bearings to study cavitation effects.

Lubricant Feed Holes

Using the continuity equation along with equation (E6), diameter of feed groove is calculated.

$$D = 0.6 \text{ mm}$$

For the purpose of changing the flow rate to produce different test conditions, the thrust bearings are designed with feed holes with diameter of 2.08 mm and internally threaded. These holes will be equipped with screw orifices to vary flow rates as needed.

The supply holes are positioned as close to the inner diameter as possible while still remaining within the water supply channel at the back of the bearing. This is done to mitigate the centrifugal effects which cause starvation of the bearing at the inner radius. The hole positioning for the slave thrust bearing is the same to ensure the bearings are identical except for the reversed taper orientations.

Lubricant Grooves

Each pad of the hydrodynamic thrust bearing has a lubricant groove along with the tapered and the land section. The main function of these grooves is to pass a quantity of lubricant. The grooves make the thrust surface appear as a series of separate pads and must be large enough to pass the required amount of lubricant. At the outside end of the radial groove, a dam is provided to control the direct leakage of lubricant from the grooves to the outside of the plate. These dams are sized to pass sufficient lubricant to maintain a 30°F temperature rise between inlet lubricants and drain lubricant. [E8]. The bearing grooves are sized based on the anticipated operating conditions.

Table 7 shows the groove dimensions

Table 7: Lubricant groove dimensions

Groove depth	0.762 mm
Groove length	16.8 mm
Groove width	3 mm
Dam width	1 mm

Bearing Geometry

Figure 23 shows the preliminary 2D drawing of the tapered land thrust bearing with basic dimensioning for the thrust bearing test rig. Table 8 shows the parameters in detail including the taper information.

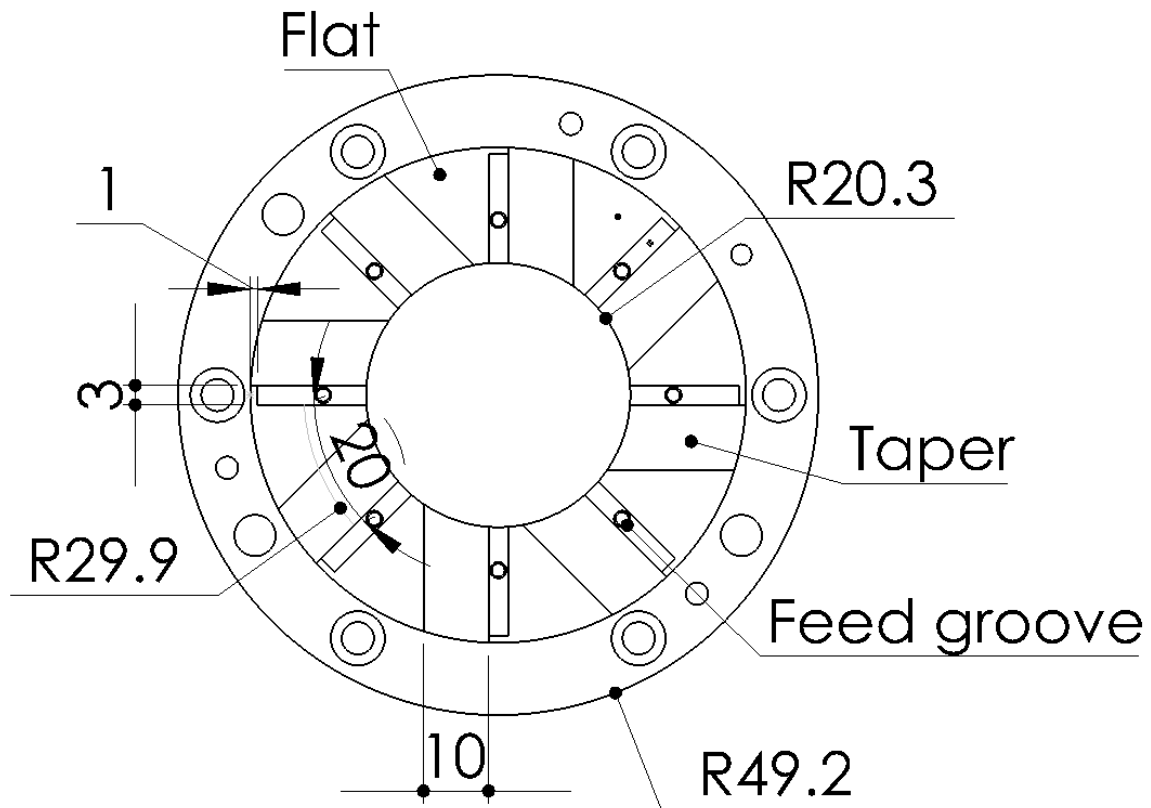


Figure 23: Preliminary Sketch for Hydrodynamic Thrust Bearing [E5] – All units in mm

Table 8: Hydrodynamic Thrust Bearings Parameters

Inner diameter [mm]	40.6
Outer diameter [mm]	76.2
Pad width [mm]	17.8
Pad Length [mm]	19.9
Taper length [mm]	10
Lubricant groove width [mm]	3
Number of pads [-]	8
Flat area [mm ²]	2839
Resting area [mm ²]	1415
Taper height [mm]	0.05
Rotation [-]	One direction

The inner and outer diameter of the bearing is sized for installation on the existing test rig. The bearing face is divided into eight equal pads. Each pad has a tapered region, a land region and a lubricant groove. The arc extent of the pad is 19.9 mm at the mean diameter of the bearing. The bearing can rotate in only one direction depending on the direction of the taper.

For load capacity, it is necessary to machine a profile in to the bearings, which generates a fluid film [E1]. Each pad has a section with a straight taper profile that makes this a slider-type bearing [E4]. This tapered wedge has a height difference that creates a pressure rise across the tapered section of the pad, which eventually draws the fluid inside and creates a fluid film.

Operating Conditions

Hydrodynamic thrust bearings rely on the hydrodynamic effect to provide axial load support. Therefore, they have no resistance to load without rotational speed of the collar.

In fixed geometry thrust bearings, a fixed inclination is selected to give an optimum performance at a specific set of operating conditions. Significant deviation from the anticipated operating conditions will reduce the effectiveness of the bearing, although, it provides significant load capacity over a reasonable operating condition range [E2]. The hydrodynamic bearing is designed for rotor speeds up to 9000 RPM. Figures 24 shows prediction plots of film thickness and flow rate, with respect to rotor speed. These trends are obtained from the prediction tool XLHydroThrust® for a constant specific static load.

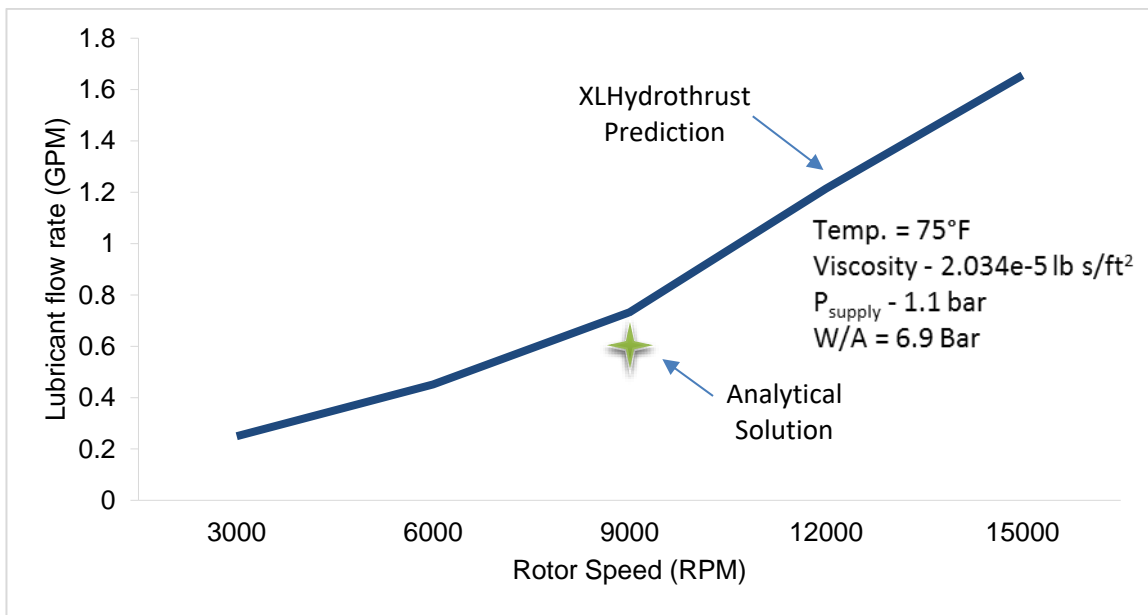
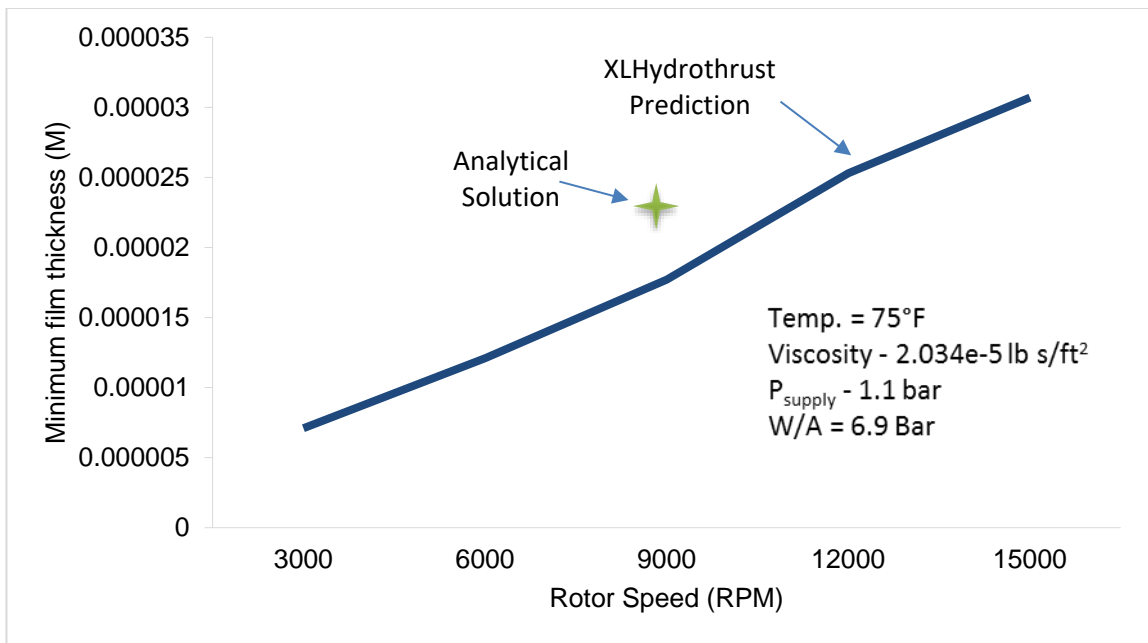


Figure 24: Minimum Film Thickness and Lubricant Flow Rate Plots vs Rotor Speed for Hydrodynamic Test Thrust Bearing

Figures 24 show that at higher speed, film thickness and flow rate of water increases for a constant specific load. However, there are other constraints that limit the operating speeds of the test rig. In the current state of the test rig, we are limited to speeds of up to 9000 RPM.

SolidWorks Models

Based on the design detailed above, SolidWorks models are created for both slave and test thrust bearings. Figure 25 shows the rendered SolidWorks model of the test thrust bearing and the slave thrust bearing respectively. These models include both the bearing face and the bearing flange. The holes in the bearing flange are made to cater the proximity probes and bolts to mount the bearing. The test thrust bearing has small openings in a groove and land region respectively, to measure the pressure at these two locations.

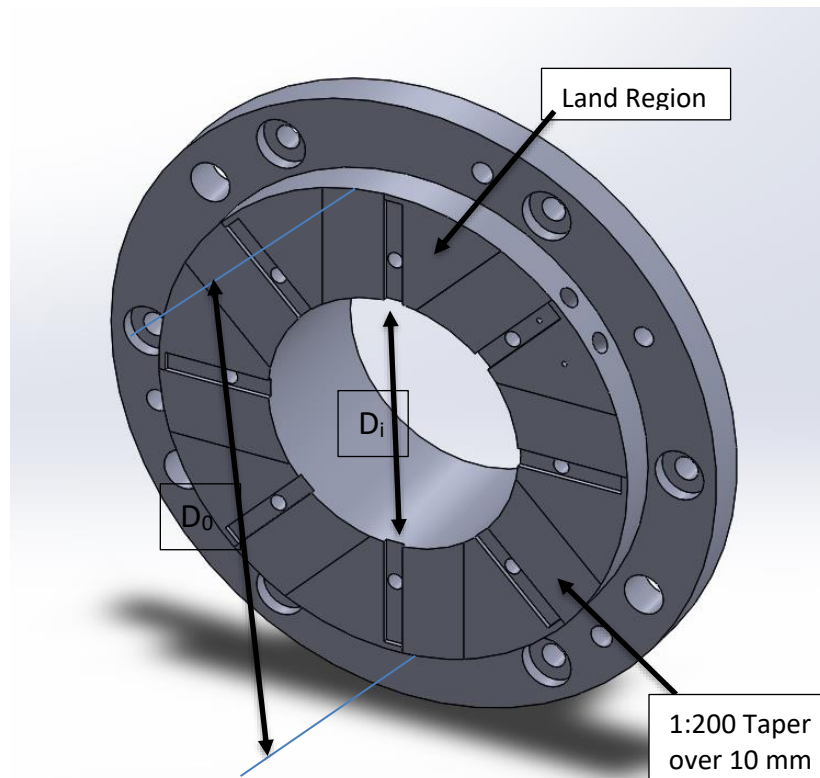


Figure 25: Test Thrust Bearing SolidWorks Model

Manufacturing Drawings

SolidWorks models are used to create thrust bearing detailed drawings for the manufacturer. Figure 26 shows the detail drawings of the test thrust bearings. These drawings included necessary details required by the manufacturers including taper detail, tolerances and surface finish. Tolerances and surface finishes are based on the ASME dimensioning and tolerancing Y14.5 code [E10]. Hole callouts are used to specify the types of holes (threaded or plain) in the bearing's flanges and bearing face.

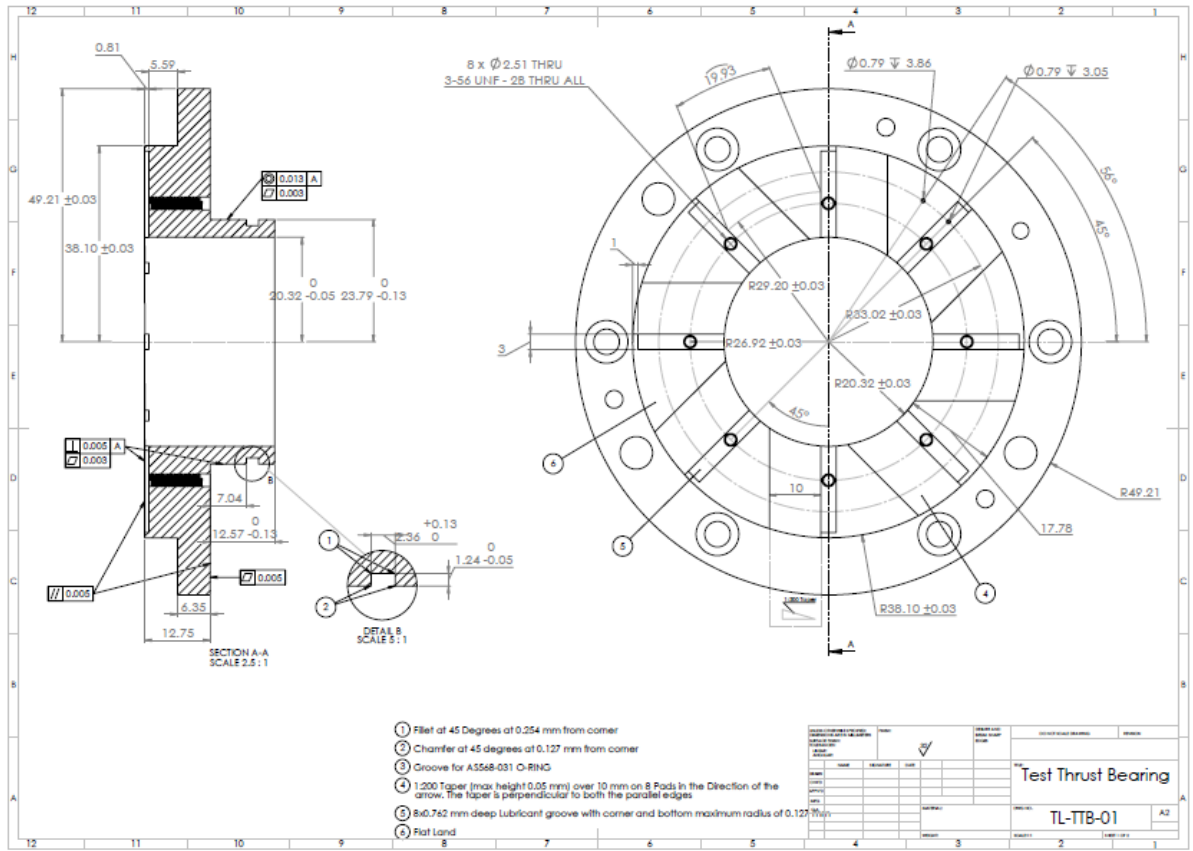


Figure 26: Test Thrust Bearing Detail Drawings

REFERENCES

- [E1] A. Leopard, 1977 "Principles of Fluid Film Bearing Design and Applications," Proceedings of the Sixth Turbomachinery Symposium, 1977.
- [E2] Abramovitz, Stanley, 1972 "Fluid Film Bearing Design Considerations." Proceedings of the First Turbomachinery Symposium, 1972.
- [E3] Loy, X., and Sinha, S., 2012, "Lubrication of polyether ether ketone (PEEK) surface by liquid ultrathin films for high wear durability", *Wear*, **296**(1-2), pp. 681-692.
- [E4] San Andrés, L., 2010, "Modern Lubrication Theory, One Dimensional Fluid Film Bearings," Notes 2-Appendix, Texas A&M University Digital Libraries, <http://hdl.handle.net/1969.1/93254> [5 April 2016].
- [E5] Eckhard Schuler, 2016, R&D Engineer, John Crane, private communication
- [E6] Fillon, M., DeCamillo, S., and Dadouche, A., 2013, "Hydrodynamic Fixed Geometry Thrust Bearings", *Encyclopedia of Tribology*, J. Wang, ed., Springer, pp. 1718-1729.
- [E7] 2017, "Slider Bearings", Universidade Federal do Amazonas - Início [Online]. Available: http://home.ufam.edu.br/berti/nanomateriais/8403_PDF_CH27.pdf. [Accessed: 24- Mar- 2017].
- [E8] 2017, "Lubrication Concepts - Industrial Wiki - odesie by Tech Transfer", Myodesie.com [Online]. Available:
- [E9] San Andrés, L., 2013, "A Test Rig for Evaluation of Thrust Bearings and Face Seals," Proposal to the Turbomachinery Research Consortium, Turbomachinery Laboratory, Texas A&M University, College Station, TX.
- [E10] Meadows, J., 2009, *Geometric dimensioning and tolerancing*, James D. Meadows, Hendersonville [Tennessee].
- [E11] Frêne, J., 1997, *Hydrodynamic lubrication*, Elsevier, Amsterdam.
- [E12] Khonsari, M., and Booser, E., 2008, *Applied tribology*, Wiley, Chichester, England.

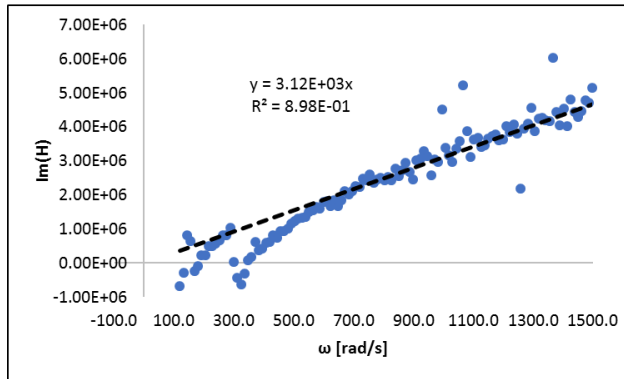
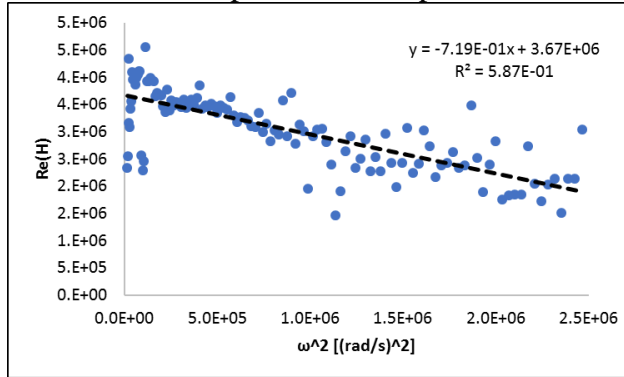
Appendix E: Thrust Bearing Dynamic Coefficient Plots

This section presents the real and imaginary plots of the impedance function used to determine the thrust bearing force parameters presented earlier in the report. Test parameters common to all the plots are listed below.

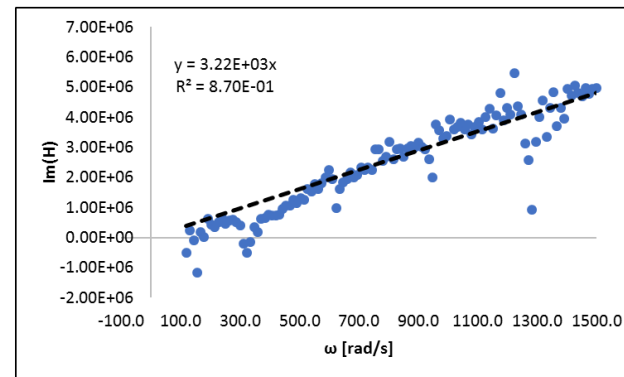
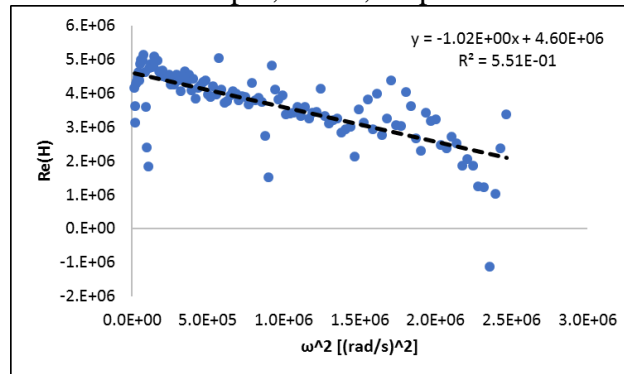
- Journal bearing supply: 50 psi(g)
- Frequency Range: 0-250 Hz
- Sampling Frequency: 31,250 Hz
- Number of Samples: 16,386
- Number of averages: 100
- Weight of Loader: 1.6094 kg
- Stiffness of Cable: 93147 N

Variable Rotor Speed Tests

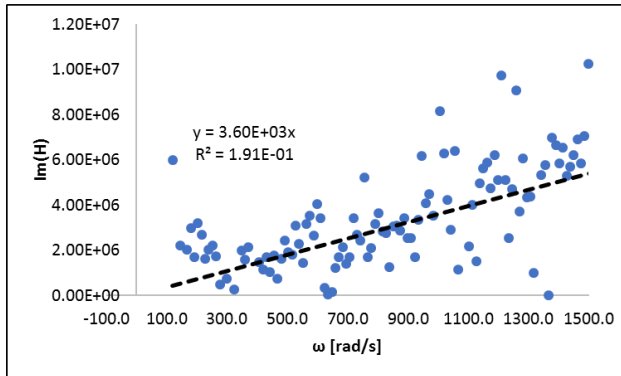
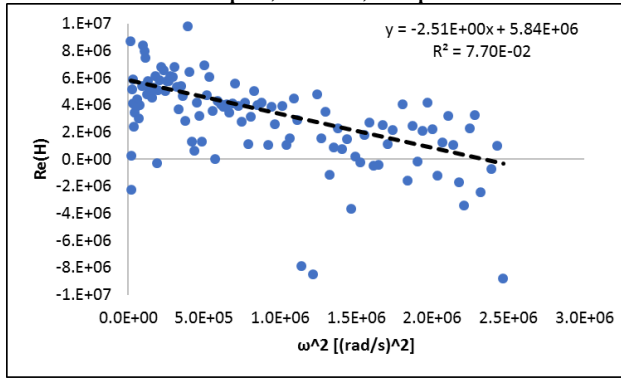
3krpm, 40 lbf, 70 psi



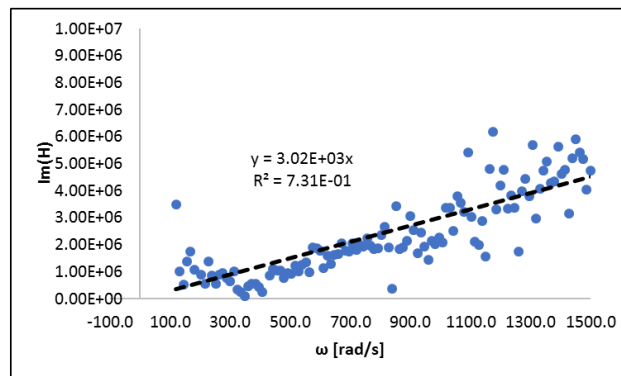
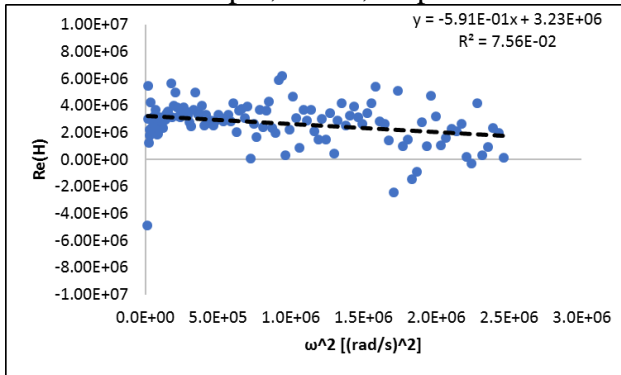
3krpm, 50 lbf, 70 psi



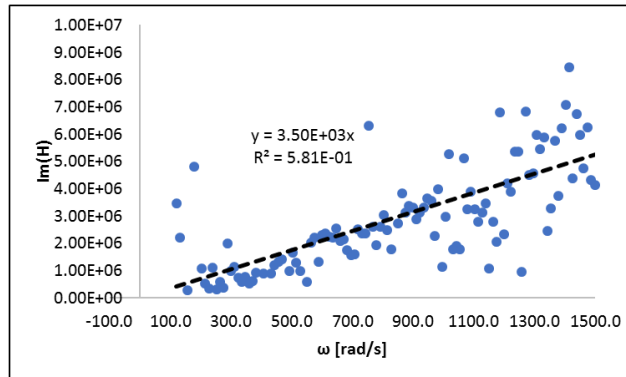
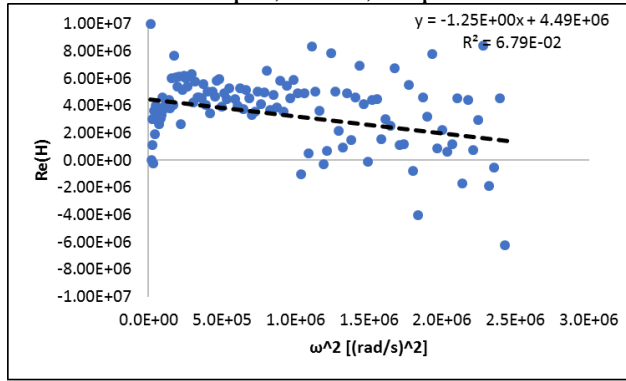
3krpm, 60 lbf, 70 psi



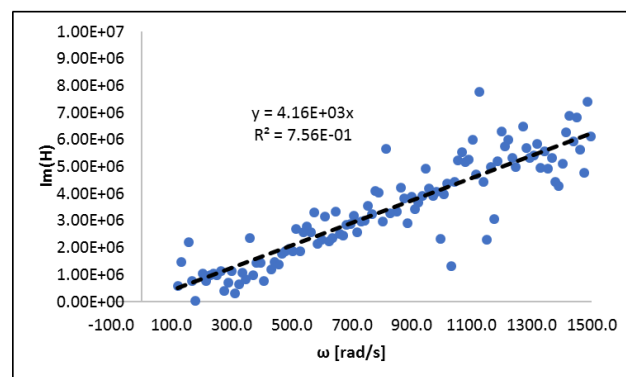
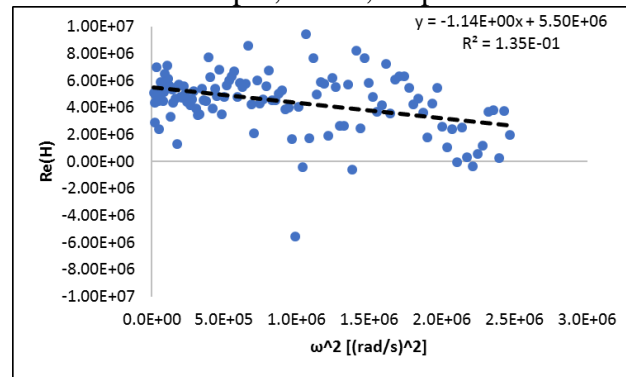
4krpm, 40 lbf, 70 psi



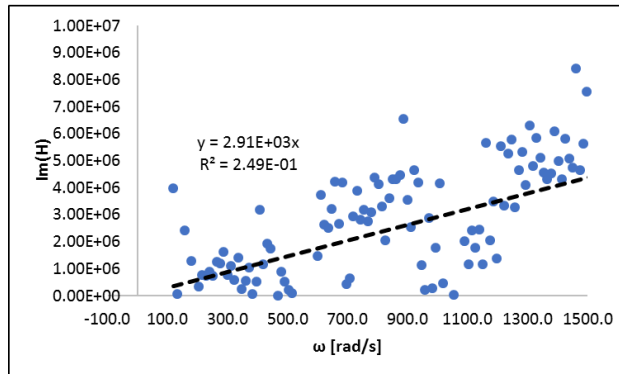
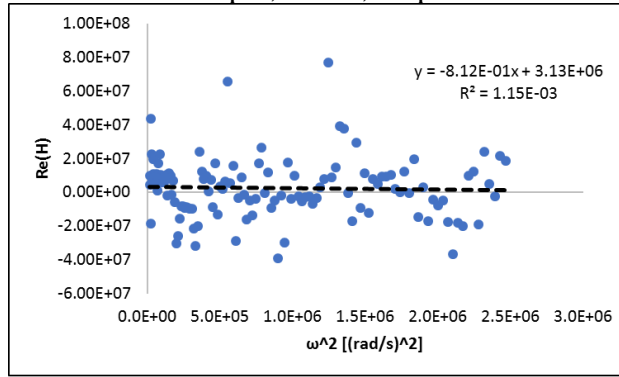
4krpm, 50 lbf, 70 psi



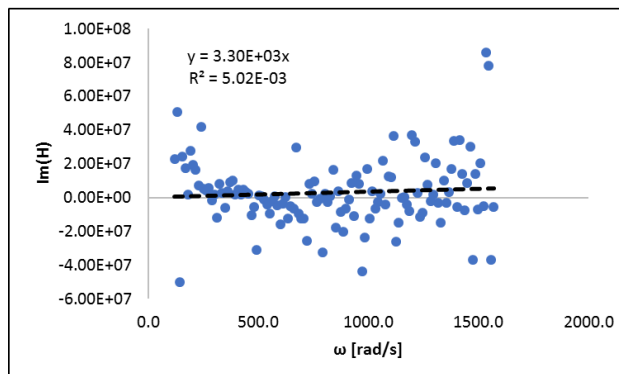
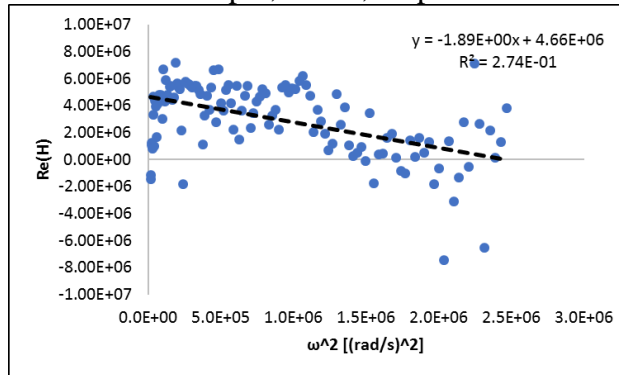
4krpm, 60 lbf, 70 psi



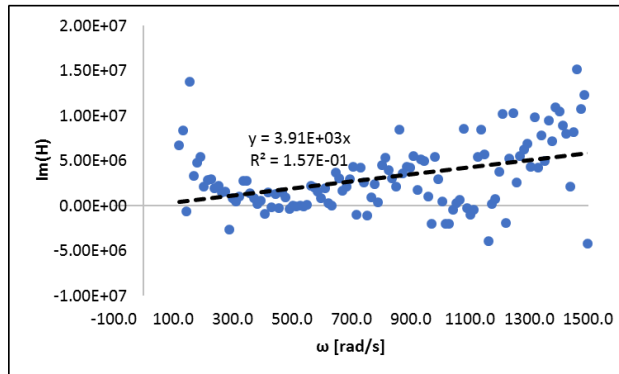
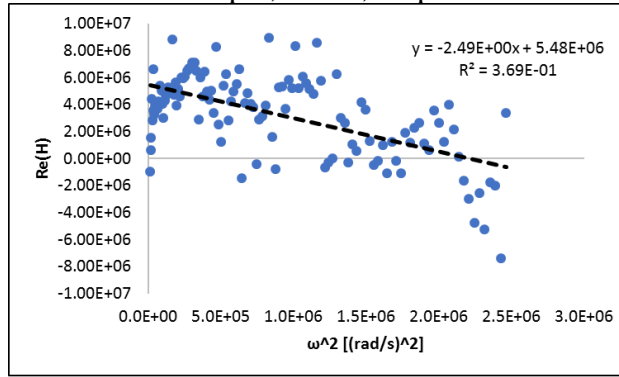
5krpm, 40 lbf, 70 psi



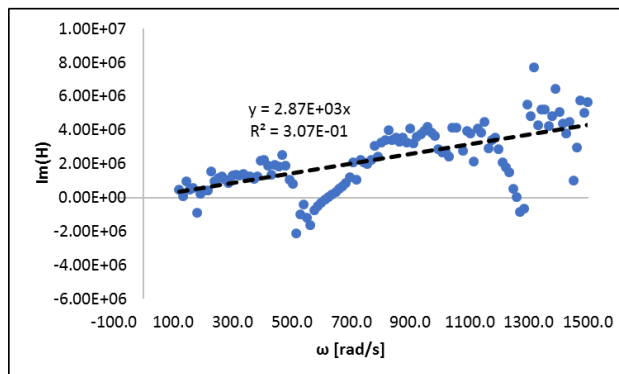
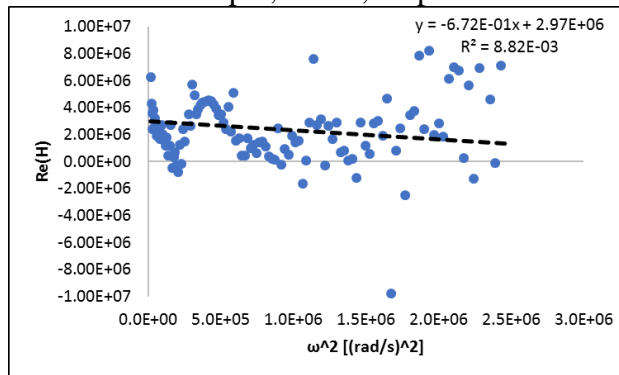
5krpm, 50 lbf, 70 psi



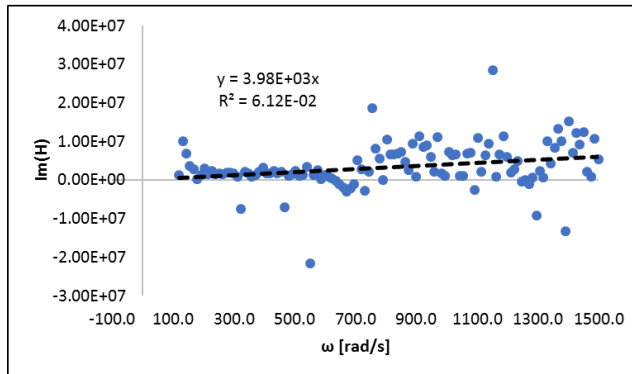
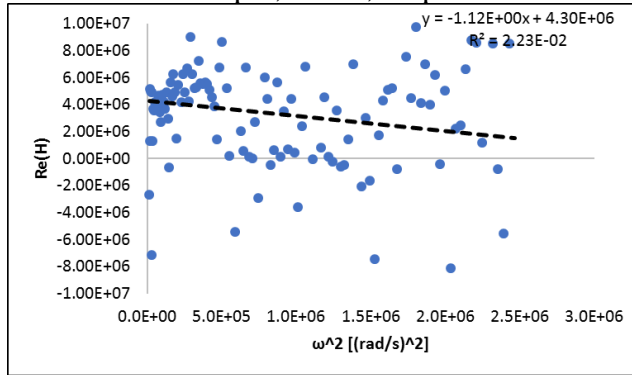
5krpm, 60 lbf, 70 psi



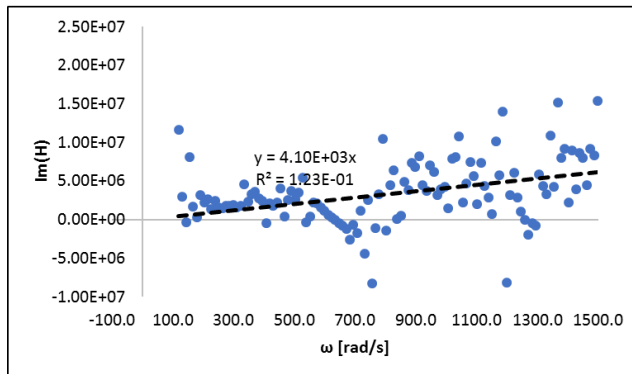
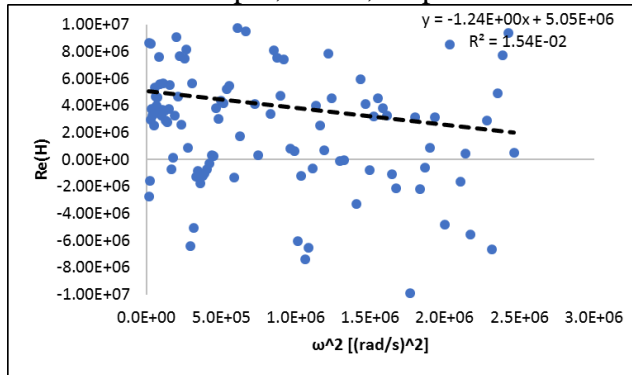
6krpm, 40 lbf, 70 psi



6krpm, 50 lbf, 70 psi

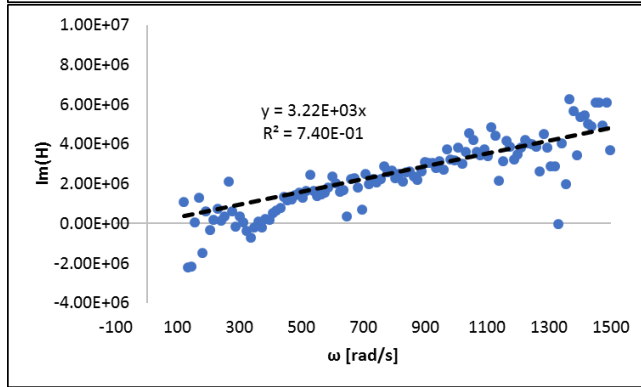
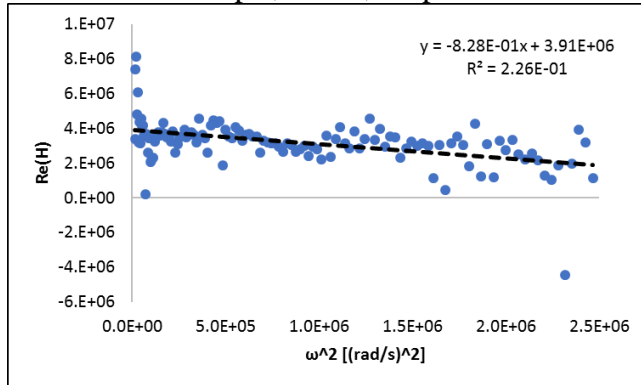


6krpm, 60 lbf, 70 psi

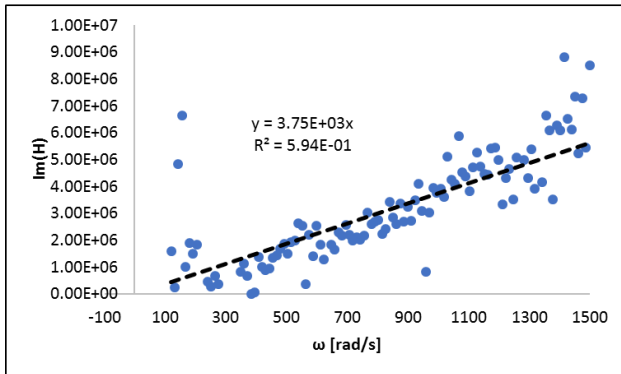
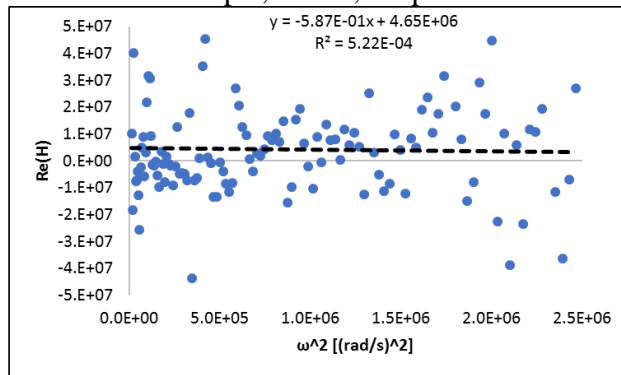


Variable Thrust Bearing Supply Pressure

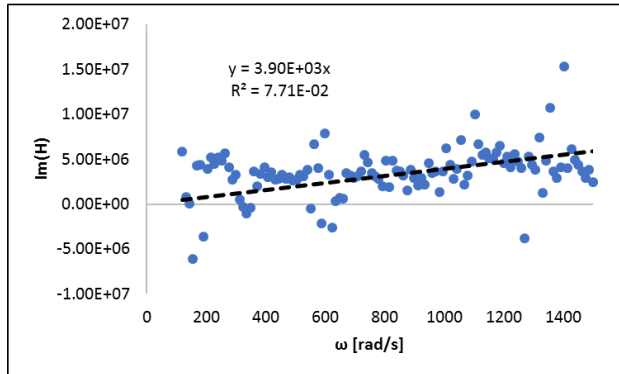
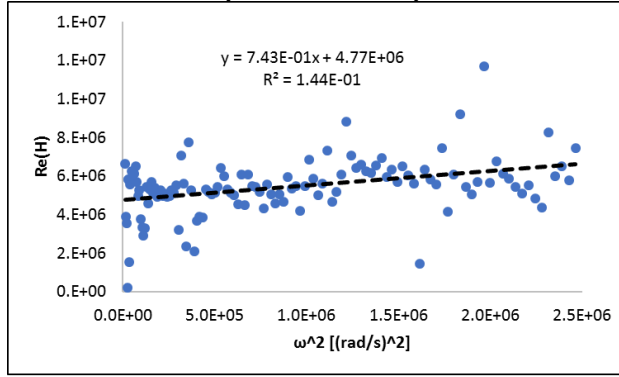
40 psi, 40 lbf, 3krpm



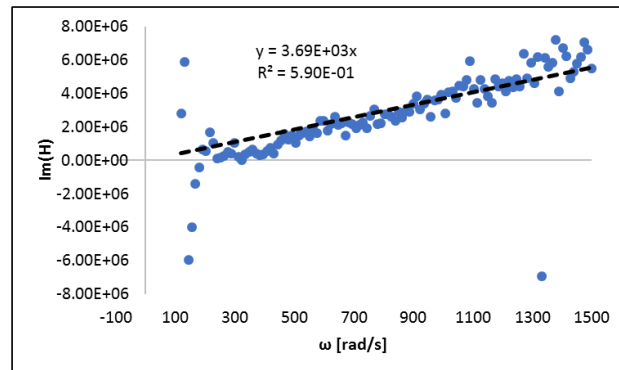
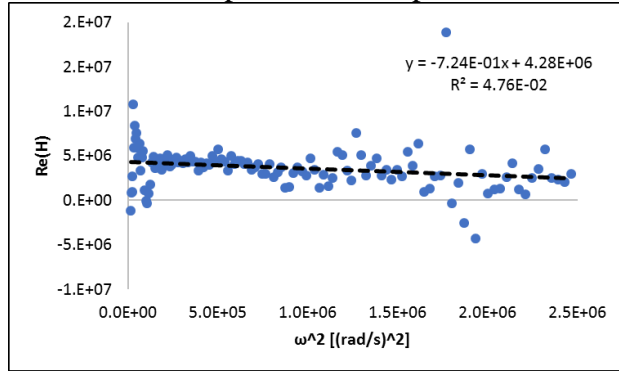
40 psi, 50 lbf, 3krpm



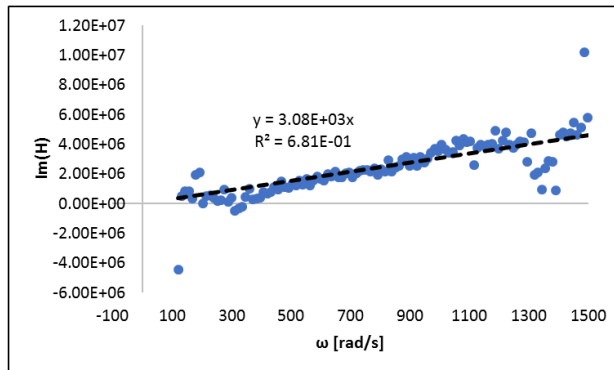
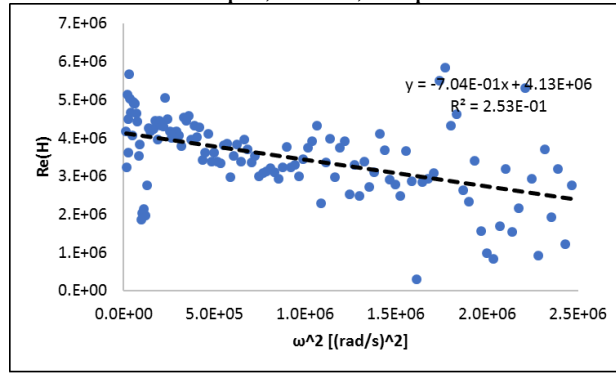
40 psi, 60 lbf, 3krpm



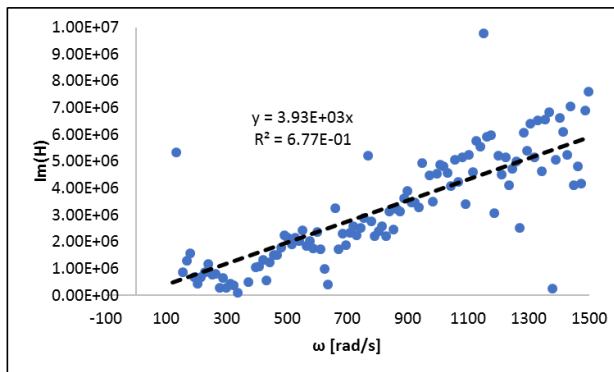
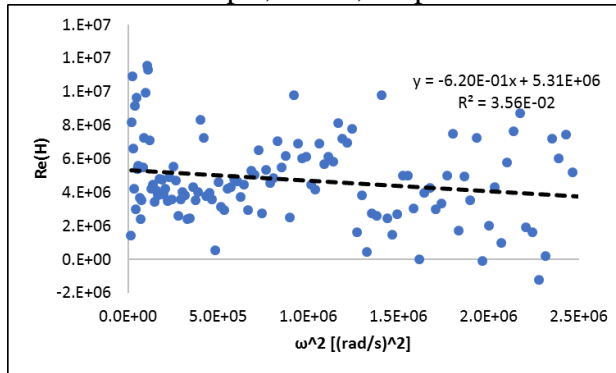
50 psi, 40 lbf, 3krpm



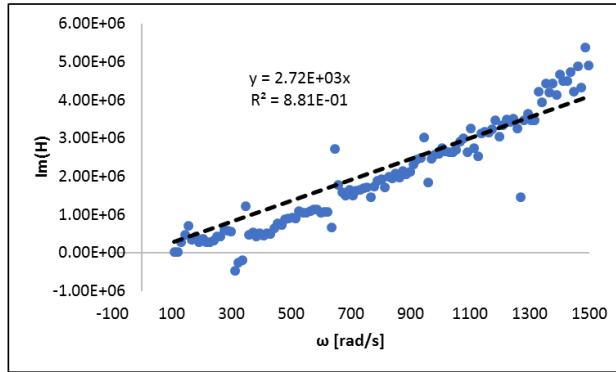
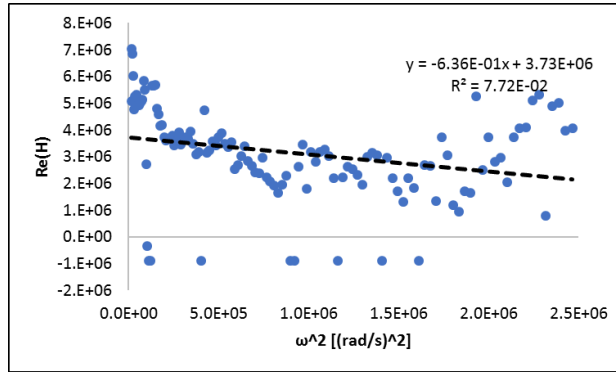
50 psi, 50 lbf, 3krpm



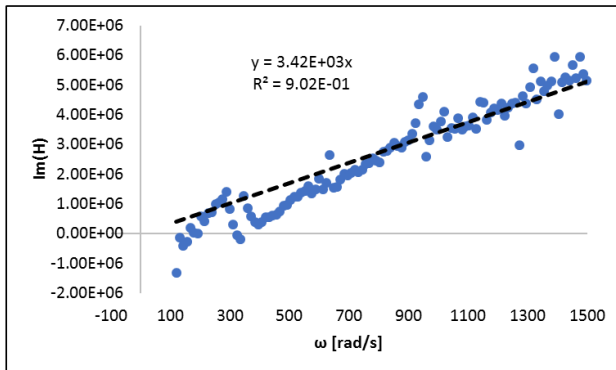
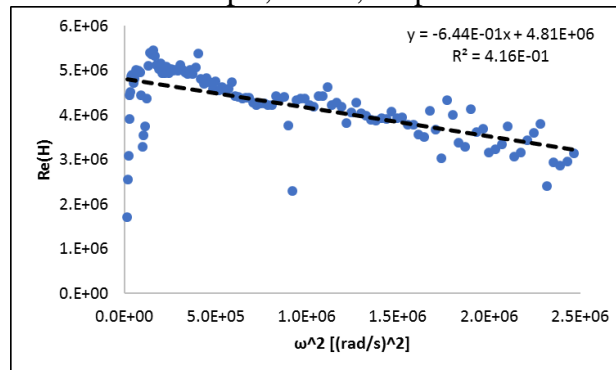
50 psi, 60 lbf, 3krpm



60 psi, 40 lbf, 3krpm



60 psi, 50 lbf, 3krpm



60 psi, 60 lbf, 3krpm

